

# Distributed model order reduction of a model for microtubule-based cell polarization using HAPOD\*

Tobias Leibner<sup>1</sup>, Maja Matis<sup>b</sup>, Mario Ohlberger<sup>1</sup>, Stephan Rave<sup>1</sup>

<sup>a</sup>*Faculty of Mathematics and Computer Science, University of Münster, Einsteinstrasse 62, 48149 Münster, tobias.leibner@uni-muenster.de, mario.ohlberger@uni-muenster.de, stephan.rave@uni-muenster.de*

<sup>b</sup>*Institute of Cell Biology, Center for Molecular Biology of Inflammation, University of Münster, Von-Esmarch-Strasse 56, 48149 Münster, matism@uni-muenster.de*

---

## Abstract

In this contribution we investigate in mathematical modeling and efficient simulation of biological cells with a particular emphasis on effective modeling of structural properties that originate from active forces generated from polymerization and depolymerization of cytoskeletal components. In detail, we propose a nonlinear continuum approach to model microtubule-based forces which have recently been established as central components of cell mechanics during early fruit fly wing development. The model is discretized in space using the finite-element method. Although the individual equations are decoupled by a semi-implicit time discretization, the discrete model is still computationally demanding. In addition, the parameters needed for the effective model equations are not easily available and have to be estimated or determined by repeatedly solving the model and fitting the results to measurements. This drastically increases the computational cost. Reduced basis methods have been used successfully to speed up such repeated solves, often by several orders of magnitude. However, for the complex nonlinear models regarded here, the application of these model order reduction methods is not always straight-forward and comes with its own set of challenges. In particular, subspace construction using the Proper Orthogonal Decomposition (POD) becomes prohibitively expensive for reasonably fine grids. We thus propose to combine the Hierarchical Approximate POD, which is a general, easy-to-implement approach to compute an approximate POD, with an Empirical Interpolation Method to efficiently generate a fast to evaluate reduced order model. Numerical experiments are given to demonstrate the applicability and efficiency of the proposed modeling and simulation approach.

---

## 1. Introduction

Cells are often called the “smallest unit of life”, as all living creatures are composed of these small entities. Notwithstanding their size, cells are incredibly complex biological machines. This is reflected in the fact that even after many years of research we are nowhere near having a full understanding of all the processes that run even in a single cell. The picture gets even more complicated when regarding the tissue level, where cell-cell and cell-extracellular matrix interactions have to be taken into account. Coarse-grained models try to remove some of the complexity by looking at the cell from a macroscopic view point, averaging over the microscopic details to focus on the essential features. Although these models are much simpler than full microscopic models they are often still very demanding computationally. In addition, the parameters needed for the model equations are often not available and have to be estimated or determined by repeatedly solving the model and comparing the results to measurements, which drastically increases the computational cost.

---

\*This is an early draft, numerical experiments are missing and there are probably many errors or inconsistencies.

In this contribution we focus on effective mathematical modeling of cytoskeletal proteins as the main source of forces that determine the shape of biological cells and tissues. While actin-based forces are thoroughly investigated, forces originating from other cytoskeletal components came into focus only recently. More specifically, we propose to use a nonlinear continuum approach [19, 31, 37, 53] to model microtubule-based forces which have recently been established as central components of cell mechanics during early fruit fly wing development [49].

While there is a broad discussion on continuous versus discrete mathematical modeling approaches for cell metamorphosis [2, 10, 14, 29], we concentrate here on the development of efficient numerical discretization and model order reduction methods for the parameterized system of coupled non-linear partial differential equations resulting from this continuum approach. To this end, the mathematical model is discretized in space using the finite-element method (FEM). Although the individual equations are decoupled by a semi-implicit time discretization, the discrete model is still very demanding computationally. This is particularly a problem since computational studies to identify effective parameters of the model require many evaluations of the finite element system with different parameter settings and thus involve a large amount of time and experimental effort. Reduced basis methods have been used successfully to speed up such repeated solves, often by several orders of magnitude. For an overview on recent developments in model order reduction, in general, and the reduced basis method, in particular, we refer to the monographs and collections [4, 5, 27, 45].

For time-dependent problems, the POD-Greedy method [24] has been established as a standard method for reduced basis constructions. However, for an efficient implementation of the POD-Greedy method, rigorous and cheap a posteriori error estimates have to be available. As this is not the case for the non-linear cell model at hand, we propose to speed-up a subspace construction based on the Proper Orthogonal Decomposition (POD) by employing a suitable variant of the Hierarchical Approximate POD (HAPOD) [28]. This procedure enormously reduces the so called offline-complexity of the model order reduction approach. In order to also achieve a good online-performance of the method for our non-linear system, a variant of the empirical interpolation method (EIM) [3, 13, 18] is used to efficiently compute the reduced model.

The rest of this paper is organized as follows. In Section 2 we will shortly review the biological background. In Section 3 we will specify the mathematical cell model and its discretization. In Section 4 we will present and discuss the model reduction approach. Finally, we will use the reduced model for some numerical studies in Section 5.

## 2. Biological background

A cell's shape and structural properties are largely controlled by the cytoskeleton, an interconnected network of filaments and associated proteins [21]. The filamentous proteins are often divided into three classes: intermediate filaments, microtubules, and actin filaments. Intermediate filaments are the most durable and long-lived of these three and their main function is to withstand tensile mechanical stress [1, 21]. Actin filaments and microtubules are more dynamic. They are build from small monomers that can assemble into large rod-like polymers. However, they can also rapidly disassemble again. While this applies to both actin and microtubules, the latter are particularly known for their *dynamic instability* [1], constantly assembling and then disassembling again if not stabilized by special cap proteins. Unlike intermediate filaments, actin filaments and microtubules are polar, i.e., they are asymmetric on molecular level. Specialized *motor proteins* use this polarity to actively transport cell components in a directed manner along these filaments. Motor proteins can also cross-link filaments and exert active forces by sliding filaments against each other. Most prominently, the contraction of muscle cells is achieved by a large number of parallel actin filaments that are pulled together by myosin motors [1, 51]. It is also long known that actin and myosin form the contractile ring during cytokinesis (the process that divides a cell in two) and are involved in cell motility, mechanosensing and mechanotransduction (e.g. [30, 33, 39–41, 43, 46, 47]). Moreover, they form the actomyosin cortex, a thin actin-myosin network attached to the cell membrane that plays an essential role in shaping the cell and controlling mechanical properties of the cell surface [48]

In contrast, microtubules were traditionally not viewed in the role of a force generator, partly because early studies underestimated the amount of force a microtubule can exert *in vivo* by polymerization at its plus end by about an order of magnitude [38]. Only recently microtubule-based forces gained broader attention [8, 15, 38, 49]. We will here focus on a recent study showing that microtubules play a major role in the mechanics of tissue morphogenesis during fruit fly (*Drosophila*) wing development [49].

### 3. Modelling

#### 3.1. Notation

Vectors are written in bold, lower-case notation and matrices in bold, upper-case notation.

Let  $\mathbf{A} = (\mathbf{a}_1, \dots, \mathbf{a}_d)^T \in \mathbb{R}^{d \times d}$  be a matrix with rows  $\mathbf{a}_i$  and let  $\mathbf{u}: \mathbb{R}^d \rightarrow \mathbb{R}^d$ . Then the divergence of  $\mathbf{A}$  is defined as

$$\mathbf{div} \mathbf{A} := \begin{pmatrix} \mathbf{div} \mathbf{a}_1 \\ \vdots \\ \mathbf{div} \mathbf{a}_d \end{pmatrix} \quad (3.1)$$

and the gradient of  $\mathbf{u}$  is defined as

$$\nabla \mathbf{u} := \begin{pmatrix} \frac{\partial u_1}{\partial x_1} & \cdots & \frac{\partial u_1}{\partial x_d} \\ \vdots & \vdots & \vdots \\ \frac{\partial u_d}{\partial x_1} & \cdots & \frac{\partial u_d}{\partial x_d} \end{pmatrix} \quad (3.2)$$

We define

$$(\mathbf{u} \cdot \nabla) \mathbf{u} = \sum_{i=1}^d u_i \frac{\partial}{\partial x_i} \mathbf{u}. \quad (3.3)$$

The Laplace operator is defined as

$$\Delta \mathbf{u} = \sum_{i=1}^d \frac{\partial^2}{\partial x_i^2} \mathbf{u} = \mathbf{div} \nabla \mathbf{u}. \quad (3.4)$$

Let  $(\cdot, \cdot)$  denote the  $L^2$  inner product, i.e.

$$(u, v) := \int_{\Omega} u(\mathbf{x})v(\mathbf{x})d\mathbf{x}. \quad (3.5)$$

For vector-valued functions we define

$$(\mathbf{u}, \mathbf{v}) := \int_{\Omega} \mathbf{u}(\mathbf{x}) \cdot \mathbf{v}(\mathbf{x})d\mathbf{x}. \quad (3.6)$$

For matrix-valued functions  $\mathbf{U} = (\mathbf{u}_1, \dots, \mathbf{u}_d)^T$ ,  $\mathbf{V} = (\mathbf{v}_1, \dots, \mathbf{v}_d)^T$  we define

$$(\mathbf{U}, \mathbf{V}) := \sum_{i=1}^d (\mathbf{u}_i, \mathbf{v}_i). \quad (3.7)$$

### 3.2. Derivation of model equations

We will model the cell as an active polar gel surrounded by a membrane that separates it from the surrounding extracellular fluid [32, 37, 52]. See [37] and references therein for a detailed derivation. Here, we only shortly recapitulate the important features of the model. The model uses a diffuse interface description of the cell, i.e., the cell is modelled by a phase field parameter  $\phi$  that takes on the value 1 inside the cell and  $-1$  outside with a smooth transition in the membrane region. The width of the transition region can be controlled by the model parameter  $\epsilon$ . The average orientation of the microtubules inside the cell is tracked by the vector-valued orientation field  $\mathbf{d}$ . For the fluid, we track the velocity  $\mathbf{u}$  and pressure  $p$ . For simplicity, we will assume equal density for the cytoplasm and extracellular fluid which is justified as both mainly consist of water [1].

The model equations are obtained by first stating the free energy of the system and then assuming that the system evolves according to a gradient descent of this free energy [17, 37]. The free energy

$$E(\phi, \mathbf{d}, \mathbf{u}) = E_{kin}(\mathbf{u}) + E_S(\phi) + E_d(\phi, \mathbf{d}) \quad (3.8)$$

is composed of the kinetic energy of the fluid, the membrane (or surface) energy  $E_S$  and the energy of the filament network  $E_d$ . In the following, we will state the energies and equations in non-dimensionalized form only, see [37] for details on the non-dimensionalization. The kinetic energy then simply is

$$E_{kin}(\mathbf{u}) = \frac{\text{Re}}{2} \int_X \mathbf{u}^2 \, dx \quad (3.9)$$

where  $\text{Re}$  is the well-known Reynolds number giving the ratio of inertial to viscous forces within the fluid. The surface energy reads

$$E_S(\phi) = \frac{1}{\text{Ca}} \int_X \frac{\epsilon}{2} |\nabla\phi|^2 + \frac{1}{\epsilon} W(\phi) \, dx + \frac{1}{\text{Be}} \int_X \frac{1}{2\epsilon} \left( \epsilon\Delta\phi - \frac{1}{\epsilon} W'(\phi) \right)^2 \, dx. \quad (3.10)$$

The first integral in (3.10) corresponds to a classic Cahn-Hilliard [11, 12] model where  $W(\phi) = \frac{1}{4}(\phi^2 - 1)^2$  is a double well potential with two minima at  $\pm 1$  giving the two pure ‘‘phases’’ (interior and exterior of the cell) a lower free energy than the interface region where  $\phi \in (-1, 1)$ . The second integral describes membrane bending energy by a Helfrich-type model [25, 26]. Accordingly, the capillary number  $\text{Ca}$  and the bending capillary number  $\text{Be}$  describe the ratio of viscous drag forces to surface tension forces and forces resisting bending, respectively.

The energy of the filament network is modelled as

$$E_d(\phi, \mathbf{d}) = \frac{1}{\text{Pa}} \int_X \frac{1}{2} \nabla\mathbf{d} : \nabla\mathbf{d} + \frac{c_1}{4} |\mathbf{d}|^2 \left( -2\phi + |\mathbf{d}|^2 \right) \, dx. \quad (3.11)$$

Here, the first term penalizes distortion of the filaments and promotes alignment. The polarity number  $\text{Pa}$  again characterizes the ratio between viscous forces and forces due to distortion of the filaments. The second term controlled by  $c_1$  (weakly) restricts  $\mathbf{d}$  to the interior of the cell and (weakly) enforces  $|\mathbf{d}| = 1$  inside the cell: If  $\phi < 0$ , the term has a single minimum at zero, otherwise it is again a double well potential with minima at  $\pm 1$ .

The phase field is advected with the flow and dissipates the energy by a gradient flow on the zero-average subspace of  $H^{-1}$  [20, 34], giving the phase field equations in the domain  $X$

$$\partial_t\phi + \text{div}(\mathbf{u}\phi) = \gamma\Delta\phi^\natural \quad (3.12a)$$

$$\phi^\natural = \frac{\delta E}{\delta\phi} \quad (3.12b)$$

$$\mu = \epsilon\Delta\phi - \frac{1}{\epsilon} W'(\phi) \quad (3.12c)$$

with

$$\begin{aligned}\frac{\delta E}{\delta \phi} &= \frac{\delta E_d}{\delta \phi} + \frac{\delta E_S}{\delta \phi} \\ &= -\frac{c_1}{2\text{Pa}} |\mathbf{d}|^2 + \frac{1}{\text{Be}} \left( \Delta \mu - \frac{1}{\epsilon^2} W''(\phi) \mu \right) - \frac{1}{\text{Ca}} \mu.\end{aligned}\quad (3.12d)$$

and initial and boundary conditions

$$\phi(0, \mathbf{x}) = \phi_0(\mathbf{x}) \quad \text{for all } \mathbf{x} \in X \quad (3.12e)$$

$$\frac{\partial \phi}{\partial n}(t, \mathbf{x}) = \frac{\partial \phi^\natural}{\partial n}(t, \mathbf{x}) = \frac{\partial \mu}{\partial n}(t, \mathbf{x}) = 0 \quad \text{for all } t \in [0, t_f], \mathbf{x} \in \partial X \quad (3.12f)$$

Here,  $\phi^\natural$  and  $\mu$  are helper variables introduced to write the sixth-order equation as a system of second-order equations. The phase field mobility coefficient  $\gamma$  is a model parameter that regulates the rate of entropy dissipation.

The orientation field equations are lend from liquid crystal theory:

$$\partial_t \mathbf{d} + (\nabla \mathbf{d}) \mathbf{u} + (\boldsymbol{\Omega}(\mathbf{u}) - \xi \mathbf{D}(\mathbf{u})) \mathbf{d} = -\frac{1}{\kappa} \mathbf{d}^\natural \quad (3.13a)$$

$$\mathbf{d}^\natural = \frac{\delta E}{\delta \mathbf{d}} = \frac{1}{\text{Pa}} (-c_1 \phi \mathbf{d} + c_1 (\mathbf{d} \cdot \mathbf{d}) \mathbf{d} - \Delta \mathbf{d}) \quad (3.13b)$$

with vorticity tensor

$$\boldsymbol{\Omega}(\mathbf{u}) = \frac{1}{2} (\nabla \mathbf{u}^T - \nabla \mathbf{u}), \quad (3.13c)$$

deformation tensor

$$\mathbf{D}(\mathbf{u}) = \frac{1}{2} (\nabla \mathbf{u}^T + \nabla \mathbf{u}) \quad (3.13d)$$

and initial and boundary conditions

$$\mathbf{d}(0, \mathbf{x}) = \mathbf{d}_0(\mathbf{x}) \quad \text{for all } \mathbf{x} \in X \quad (3.13e)$$

$$\frac{\partial \mathbf{d}}{\partial \mathbf{n}}(t, \mathbf{x}) = \mathbf{0} \quad \text{for all } t \in [0, t_f], \mathbf{x} \in \partial X. \quad (3.13f)$$

The filaments are advected with the flow and energy is dissipated by a  $L^2$  gradient flow with scaling factor  $\frac{1}{\kappa}$ . The shape factor  $\xi$  influences alignment of the filaments with the flow and is positive for the rod-like microtubules [35, 37].

Finally, evolution of the flow is modelled by the Navier-Stokes equations

$$\text{Re} (\partial_t \mathbf{u} + (\nabla \mathbf{u}) \mathbf{u}) + \nabla p = \mathbf{div} (\boldsymbol{\sigma}_{viscous} + \boldsymbol{\sigma}_{active} + \boldsymbol{\sigma}_{dist} + \boldsymbol{\sigma}_{ericksen}) \quad (3.14a)$$

$$\mathbf{div} \mathbf{u} = 0 \quad (3.14b)$$

where

$$\boldsymbol{\sigma}_{viscous}(\mathbf{u}) = \mathbf{D}(\mathbf{u}) = \frac{1}{2} (\nabla \mathbf{u}^T + \nabla \mathbf{u}), \quad (3.14c)$$

$$\boldsymbol{\sigma}_{active}(\phi, \mathbf{d}) = \frac{1}{\text{Fa}} \tilde{\phi} \mathbf{d} \otimes \mathbf{d}, \quad \tilde{\phi} = \frac{1}{2} (\phi + 1) \quad (3.14d)$$

$$\boldsymbol{\sigma}_{dist}(\mathbf{d}, \mathbf{d}^\natural) = \frac{1}{2} (\mathbf{d}^\natural \otimes \mathbf{d} - \mathbf{d} \otimes \mathbf{d}^\natural) + \frac{\xi}{2} (\mathbf{d}^\natural \otimes \mathbf{d} + \mathbf{d} \otimes \mathbf{d}^\natural), \quad (3.14e)$$

$$\begin{aligned}\boldsymbol{\sigma}_{ericksen}(\phi, \phi^\natural, \mathbf{d}, \mathbf{d}^\natural) &= \frac{1}{\text{Be}} (\nabla \phi \otimes \nabla \mu - \mu \nabla \nabla \phi) - \frac{1}{\text{Ca}} (\epsilon \nabla \phi \otimes \nabla \phi) \\ &\quad - \frac{1}{\text{Pa}} (\nabla \mathbf{d}^T \cdot \nabla \mathbf{d})\end{aligned}\quad (3.14f)$$

are the stresses stemming from viscosity of the fluid, active extension or contraction of the filaments, distortion of the filaments and additional stress from the energy-minimizing behavior of both filaments and membrane, respectively [37]. The active force number  $Fa$  describes the ratio of viscous forces to the active forces and is positive for contractile and negative for extensile stress. The term  $\tilde{\phi}$  serves as an indicator function for  $\phi > 0$  and thus restricts the active stress to the cytoplasm. However, as we already weakly enforce  $\mathbf{d} = 0$  outside of the cell (see above), removing this factor probably would not change the dynamics of the model significantly.

By redefining the pressure, we can simplify the divergence of the last stress term to obtain (see [36, Section 6.2.4 and Remark 3.2])

$$\mathbf{div}(\boldsymbol{\sigma}_{ericksen}(\phi, \phi^{\natural}, \mathbf{d}, \mathbf{d}^{\natural})) = \phi^{\natural} \nabla \phi + (\nabla \mathbf{d})^T \mathbf{d}^{\natural}, \quad (3.14g)$$

The equations are complemented with initial and boundary conditions

$$\mathbf{u}(0, \mathbf{x}) = \mathbf{u}_0(\mathbf{x}) \text{ for all } \mathbf{x} \in X \quad (3.14h)$$

$$\mathbf{u}(t, \mathbf{x}) = \mathbf{0} \text{ for all } t \in [0, t_f], \mathbf{x} \in \partial X. \quad (3.14i)$$

As cell motility generally occurs in a regime with very low Reynolds number, in the following, we will restrict ourselves to the Stokes approximation obtained by setting  $Re = 0$  in (3.14).

The model (3.12)-(3.14) conserves the cell volume, i.e.,

$$\partial_t \int_X \phi \, dx = 0, \quad (3.15)$$

and is thermodynamically consistent, i.e., the free energy (3.8) decreases over time

$$\partial_t E \leq 0. \quad (3.16)$$

### 3.3. Weak formulations

We will use a finite element discretization to numerically solve the model equations. To that end, we first derive weak formulations for each of the systems of equations (3.12)-(3.14).

#### 3.3.1. Phase field

Multiplying (3.12) by test functions  $(\chi, \chi^{\natural}, \nu) \in (H^1(X))^3$  and integrating gives

$$\begin{aligned} \partial_t \int_X \phi \chi \, dx + \int_{\partial X} \phi \chi \mathbf{u} \cdot \mathbf{n} - \int_X \phi \mathbf{u} \cdot \nabla \chi \, dx &= \gamma \left( \int_{\partial X} \chi \nabla \phi^{\natural} \cdot \mathbf{n} - \int_X \nabla \phi^{\natural} \cdot \nabla \chi \, dx \right) \\ \int_X \phi^{\natural} \chi^{\natural} \, dx &= \int_X \left( -\frac{c_1}{2Pa} \mathbf{d} \cdot \mathbf{d} - \left( \frac{1}{Ca} + \frac{1}{Be \cdot \epsilon^2} W''(\phi) \right) \mu \right) \chi^{\natural} \, dx \\ &\quad + \frac{1}{Be} \left( \int_{\partial X} \chi^{\natural} \nabla \mu \cdot \mathbf{n} \, dx - \int_X \nabla \mu \cdot \nabla \chi^{\natural} \, dx \right) \\ \int_X \mu \nu \, dx &= \epsilon \left( \int_{\partial X} \nu \nabla \phi \cdot \mathbf{n} \, dx - \int_X \nabla \phi \cdot \nabla \nu \, dx \right) - \int_X \frac{1}{\epsilon} W'(\phi) \nu \, dx. \end{aligned}$$

Using the boundary conditions (3.12f) and (3.14i), the boundary integrals vanish and we arrive at the weak formulation

$$\partial_t \int_X \phi \chi \, dx - \int_X (\phi \mathbf{u} - \gamma \nabla \phi^\natural) \cdot \nabla \chi \, dx = 0 \quad (3.17a)$$

$$\int_X \phi^\natural \chi^\natural + \frac{1}{\text{Be}} \nabla \mu \cdot \nabla \chi^\natural + \left( \frac{1}{\text{Ca}} + \frac{1}{\text{Be} \cdot \epsilon^2} W''(\phi) \right) \mu \chi^\natural \, dx = - \int_X \left( \frac{c_1}{2\text{Pa}} \mathbf{d} \cdot \mathbf{d} \right) \chi^\natural \, dx \quad (3.17b)$$

$$\int_X \mu \nu + \frac{1}{\epsilon} W'(\phi) \nu + \epsilon \nabla \phi \cdot \nabla \nu \, dx = 0 \quad (3.17c)$$

for  $(\phi, \phi^\natural, \mu) \in (H^1(X))^3$ .

### 3.3.2. Orientation field

Multiplying (3.13) by test functions  $(\mathbf{q}, \mathbf{q}^\natural) \in (H^1(X))^d \times (L^2(X))^d$  and integrating gives

$$\begin{aligned} 0 &= \partial_t \int_X \mathbf{d} \cdot \mathbf{q}^\natural \, dx + \int_X \left( (\nabla \mathbf{d}) \mathbf{u} + (\boldsymbol{\Omega}(\mathbf{u}) - \xi \mathbf{D}(\mathbf{u})) \mathbf{d} + \frac{1}{\kappa} \mathbf{d}^\natural \right) \cdot \mathbf{q}^\natural \, dx, \\ 0 &= \int_X \left( \mathbf{d}^\natural + \frac{c_1}{\text{Pa}} \phi \mathbf{d} - \frac{c_1}{\text{Pa}} (\mathbf{d} \cdot \mathbf{d}) \mathbf{d} \right) \cdot \mathbf{q} - \frac{1}{\text{Pa}} \nabla \mathbf{d} : \nabla \mathbf{q} \, dx \\ &\quad + \frac{1}{\text{Pa}} \int_{\partial X} (\nabla \mathbf{d} \cdot \mathbf{n}) \cdot \mathbf{q} \, dx \end{aligned}$$

Using the boundary conditions (3.13f) the last term vanishes and we arrive at the weak formulation for the orientation field variables  $(\mathbf{d}, \mathbf{d}^\natural) \in (H^1(X))^d \times (L^2(X))^d$

$$\partial_t \int_X \mathbf{d} \cdot \mathbf{q}^\natural \, dx + \int_X \left( (\nabla \mathbf{d}) \mathbf{u} + (\boldsymbol{\Omega}(\mathbf{u}) - \xi \mathbf{D}(\mathbf{u})) \mathbf{d} + \frac{1}{\kappa} \mathbf{d}^\natural \right) \cdot \mathbf{q}^\natural \, dx = 0, \quad (3.18a)$$

$$\int_X \left( \mathbf{d}^\natural + \frac{c_1}{\text{Pa}} \phi \mathbf{d} - \frac{c_1}{\text{Pa}} (\mathbf{d} \cdot \mathbf{d}) \mathbf{d} \right) \cdot \mathbf{q} - \frac{1}{\text{Pa}} \nabla \mathbf{d} : \nabla \mathbf{q} \, dx = 0 \quad (3.18b)$$

### 3.3.3. Stokes

We use a standard weak formulation [44] of the Stokes equations (3.14): Find  $(\mathbf{u}, p) \in H_0^1(X)^d \times L_0^2(X)$  such that

$$\int_X p \cdot \text{div} \mathbf{v} + \frac{1}{2} \nabla \mathbf{u} : \nabla \mathbf{v} \, dx = - \int_X (\boldsymbol{\sigma}_{active}(\phi, \mathbf{d}) + \boldsymbol{\sigma}_{dist}(\mathbf{d}, \mathbf{d}^\natural) + \boldsymbol{\sigma}_{ericksen}(\phi, \phi^\natural, \mathbf{d}, \mathbf{d}^\natural)) : \nabla \mathbf{v} \, dx \quad (3.19a)$$

$$\int_X q \text{div} \mathbf{u} \, dx = 0 \quad (3.19b)$$

for all  $(\mathbf{v}, q) \in H_0^1(X)^d \times L_0^2(X)$ . Note that

$$\begin{aligned} \text{div}(\boldsymbol{\sigma}_{viscous}) &= \text{div} \left( \frac{1}{2} (\nabla \mathbf{u} + (\nabla \mathbf{u})^T) \right) = \frac{1}{2} (\Delta \mathbf{u} + \text{div}((\nabla \mathbf{u})^T)) \\ &= \frac{1}{2} (\Delta \mathbf{u} + \nabla(\text{div} \mathbf{u})) = \frac{1}{2} \Delta \mathbf{u} \end{aligned}$$

due to the incompressibility constraint on the fluid, which after partial integration gives the second term on the left-hand side of (3.19a). Moreover, we used the fact that

$$\begin{aligned} \int_X \mathbf{div}(\mathbf{A}) \cdot \mathbf{v} \, dx &= \int_X \sum_{k=0}^{d-1} \mathbf{div}(\mathbf{a}_k) v_k \, dx \\ &= \int_{\partial X} \sum_{k=0}^{d-1} v_k \mathbf{a}_k \cdot \mathbf{n} \, dx - \int_X \sum_{k=0}^{d-1} \mathbf{a}_k \cdot \nabla v_k \, dx \\ &= - \int_X \mathbf{A} : \nabla \mathbf{v} \, dx \end{aligned}$$

for any matrix  $\mathbf{A}$  (here, the boundary integrals vanish since  $\mathbf{v} \in H_0^1(X)$ ).

For the Ericksen stress, instead of performing the partial integration, we will usually use the reformulation (3.14g) and thus directly use the term

$$\int_X \mathbf{div}(\boldsymbol{\sigma}_{ericksen}(\phi, \phi^\natural, \mathbf{d}, \mathbf{d}^\natural)) \cdot \mathbf{v} \, dx \quad (3.20)$$

on the right-hand side of (3.19).

#### 3.4. Finite element discretization

For the space discretization, we use a standard Galerkin finite element discretization. For simplicity, we use the same approximation order  $p$  for the phase field variables, the orientation field variables and the Stokes pressure. We use Taylor-Hood elements to discretize the Stokes equations, i.e., the approximation order for the Stokes velocity is chosen to be  $p + 1$ .

Let  $V_h^p \subset H^1(X) \subset L^2(X)$  be the continuous finite element approximation spaces with polynomial order  $p$  and grid width  $h$ , and let  $V_{h,0}^p \subset V_h^p \cap H_0^1$  be the space of functions in  $V_h^p$  that are zero on the Dirichlet boundary. Let  $\varphi_1, \dots, \varphi_{n_h^p}$  be a basis of  $V_h^p$  and  $\boldsymbol{\varphi}_1, \dots, \boldsymbol{\varphi}_{(n_h^p)^d}$  be a basis of  $(V_h^p)^d$ . Moreover, let  $\boldsymbol{\psi}_1, \dots, \boldsymbol{\psi}_{(n_{h,0}^{p+1})^d}$  be a basis of  $(V_{h,0}^{p+1})^d$ . We then write the finite element approximations of our variables as  $\phi_h = \sum_{i=1}^{n_h^p} \underline{\phi}_i \varphi_i$ ,  $\phi_h^\natural = \sum_{i=1}^{n_h^p} \underline{\phi}_i^\natural \varphi_i$ ,  $\mu_h = \sum_{i=1}^{n_h^p} \underline{\mu}_i \varphi_i$ ,  $\mathbf{d}_h = \sum_{i=1}^{(n_h^p)^d} \underline{\mathbf{d}}_i \boldsymbol{\varphi}_i$ ,  $\mathbf{d}_h^\natural = \sum_{i=1}^{(n_h^p)^d} \underline{\mathbf{d}}_i^\natural \boldsymbol{\varphi}_i$ ,  $\mathbf{u}_h = \sum_{i=1}^{(n_{h,0}^{p+1})^d} \underline{\mathbf{u}}_i \boldsymbol{\psi}_i$  and  $p_h = \sum_{i=1}^{n_h^p} \underline{p}_i \varphi_i$  with corresponding coefficient vectors  $\underline{\phi}, \underline{\phi}^\natural, \underline{\mu}, \underline{\mathbf{p}} \in \mathbb{R}^{n_h^p}$ ,  $\underline{\mathbf{d}}, \underline{\mathbf{d}}^\natural \in \mathbb{R}^{(n_h^p)^d}$  and  $\underline{\mathbf{u}} \in \mathbb{R}^{(n_{h,0}^{p+1})^d}$ .

##### 3.4.1. Phase field

Inserting these basis representations in (3.17) gives the system

$$\partial_t \mathbf{M}_{pf} \underline{\phi} - \mathbf{B}(\mathbf{u}_h) \underline{\phi} + \gamma \mathbf{E} \underline{\phi}^\natural = \mathbf{0} \quad (3.21a)$$

$$\frac{1}{\text{Be} \cdot \epsilon^2} \mathbf{f}(\phi_h, \mu_h) + \mathbf{M}_{pf} \underline{\phi}^\natural + \left( \frac{1}{\text{Ca}} \mathbf{M}_{pf} + \frac{1}{\text{Be}} \mathbf{E} \right) \underline{\mu} = - \frac{c_1}{2\text{Pa}} \mathbf{a}(\mathbf{d}_h) \quad (3.21b)$$

$$\frac{1}{\epsilon} \mathbf{g}(\phi_h) + \epsilon \mathbf{E} \underline{\phi} + \mathbf{M}_{pf} \underline{\mu} = \mathbf{0} \quad (3.21c)$$

with

$$\begin{aligned}
\mathbf{M}_{pf} &\in \mathbb{R}^{n_h^p \times n_h^p} \text{ s.t. } M_{ij} = \int_X \varphi_i \varphi_j \, dx \\
\mathbf{B}(\mathbf{u}) &\in \mathbb{R}^{n_h^p \times n_h^p} \text{ s.t. } B_{ij} = \int_X (\mathbf{u} \cdot \nabla \varphi_i) \varphi_j \, dx \\
\mathbf{E} &\in \mathbb{R}^{n_h^p \times n_h^p} \text{ s.t. } K_{ij} = \int_X \nabla \varphi_i \cdot \nabla \varphi_j \, dx \\
\mathbf{f}(\phi, \mu) &\in \mathbb{R}^{n_h^p} \text{ s.t. } f_i(\phi, \mu) = \int_X W''(\phi) \mu \varphi_i \, dx \\
\mathbf{g}(\phi) &\in \mathbb{R}^{n_h^p} \text{ s.t. } g_i(\phi) = \int_X W'(\phi) \varphi_i \, dx \\
\mathbf{a}(\mathbf{d}) &\in \mathbb{R}^{n_h^p} \text{ s.t. } a_i(\mathbf{d}) = \int_X (\mathbf{d} \cdot \mathbf{d}) \varphi_i \, dx
\end{aligned}$$

### 3.4.2. Orientation field

Inserting the basis representations in (3.18) gives the system

$$\partial_t \mathbf{M}_{of} \underline{\mathbf{d}} + \mathbf{B}(\mathbf{u}) \underline{\mathbf{d}} + \frac{1}{\kappa} \mathbf{M}_{of} \underline{\mathbf{d}}^{\mathfrak{h}} = \mathbf{0} \quad (3.22a)$$

$$\mathbf{M}_{of} \underline{\mathbf{d}}^{\mathfrak{h}} + \frac{c_1}{\text{Pa}} \mathbf{C}(\phi_h) \underline{\mathbf{d}} - \frac{c_1}{\text{Pa}} \mathbf{f}(\mathbf{d}_h) - \frac{1}{\text{Pa}} \mathbf{E} \underline{\mathbf{d}} = \mathbf{0} \quad (3.22b)$$

with

$$\begin{aligned}
\mathbf{M}_{of} &\in \mathbb{R}^{(n_h^p)^d \times (n_h^p)^d} \text{ s.t. } M_{ij} = \int_X \varphi_i \cdot \varphi_j \, dx \\
\mathbf{E} &\in \mathbb{R}^{(n_h^p)^d \times (n_h^p)^d} \text{ s.t. } K_{ij} = \int_X \nabla \varphi_i : \nabla \varphi_j \, dx \\
\mathbf{B}(\mathbf{u}) &\in \mathbb{R}^{(n_h^p)^d \times (n_h^p)^d} \text{ s.t. } B_{ij} = \int_X \left( (\nabla \varphi_j) \mathbf{u} + (\boldsymbol{\Omega}(\mathbf{u}) - \xi \mathbf{D}(\mathbf{u})) \varphi_j \right) \cdot \varphi_i \, dx \\
\mathbf{C}(\phi) &\in \mathbb{R}^{(n_h^p)^d \times (n_h^p)^d} \text{ s.t. } C_{ij}(\phi) = \int_X \phi \varphi_i \cdot \varphi_j \, dx \\
\mathbf{f}(\mathbf{d}) &\in \mathbb{R}^{(n_h^p)^d} \text{ s.t. } f_i(\mathbf{d}) = \int_X (\mathbf{d} \cdot \mathbf{d}) \mathbf{d} \cdot \varphi_i \, dx
\end{aligned}$$

### 3.4.3. Stokes

The discretized Stokes system reads

$$\mathbf{A} \underline{\mathbf{u}} + \mathbf{B}^T \underline{\mathbf{p}} = \mathbf{a} \left( \phi_h, \phi_h^{\mathfrak{h}}, \mathbf{d}_h, \mathbf{d}_h^{\mathfrak{h}} \right) \quad (3.23a)$$

$$\mathbf{B} \underline{\mathbf{u}} = \mathbf{0} \quad (3.23b)$$

where

$$\begin{aligned} \mathbf{A} &\in \mathbb{R}^{(n_{h,0}^{p+1})^d \times (n_{h,0}^{p+1})^d} \text{ s.t. } A_{ij} = \frac{1}{2} \int_X \nabla \psi_i : \nabla \psi_j \, dx \\ \mathbf{B} &\in \mathbb{R}^{n_h^p \times (n_{h,0}^{p+1})^d} \text{ s.t. } B_{ij} = \int_X \varphi_i \operatorname{div} \psi_j \, dx \\ \mathbf{a}(\phi, \phi^{\natural}, \mathbf{d}, \mathbf{d}^{\natural}) &\in \mathbb{R}^{(n_{h,0}^{p+1})^d} \text{ s.t. } a_i = \int_X \operatorname{div} (\boldsymbol{\sigma}_{ericksen}(\phi, \phi^{\natural}, \mathbf{d}, \mathbf{d}^{\natural})) \cdot \psi_i \, dx \\ &\quad - \int_X (\boldsymbol{\sigma}_{active}(\phi, \mathbf{d}) + \boldsymbol{\sigma}_{dist}(\mathbf{d}, \mathbf{d}^{\natural})) : \nabla \psi_i \, dx \end{aligned}$$

### 3.5. Time discretization

Exactly as [37], we use a semi-implicit splitting scheme to decouple the phase field, orientation field and flow equations. We introduce a partition  $0 = t_0 < t_1 < \dots < t_K = t_f$  of the time interval  $[0, t_f]$ . For simplicity, we will use a fixed time step  $\Delta t$ , i.e.,  $t^k = k\Delta t$ . We will indicate the variables at the discrete times by superscripts, e.g.,  $\phi^k(\mathbf{x}) \approx \phi(t^k, \mathbf{x})$  is the approximation of the phase field  $\phi$  at time  $t^k$ . In each time step, we first solve the phase field equations (3.21) where we discretize the phase field variables implicitly and the other variables explicitly.

$$(\mathbf{M}_{pf} - \Delta t \mathbf{B}(\mathbf{u}_h^k)) \underline{\phi}^{k+1} + \Delta t \gamma \mathbf{E} \underline{\phi}^{\natural, k+1} = \mathbf{M}_{pf} \underline{\phi}^k \quad (3.24a)$$

$$\frac{1}{\operatorname{Be} \cdot \epsilon^2} \mathbf{f}(\phi_h^{k+1}, \mu_h^{k+1}) + \mathbf{M}_{pf} \underline{\phi}^{\natural, k+1} + \left( \frac{1}{\operatorname{Ca}} \mathbf{M}_{pf} + \frac{1}{\operatorname{Be}} \mathbf{E} \right) \underline{\boldsymbol{\mu}}^{k+1} = -\frac{c_1}{2\operatorname{Pa}} \mathbf{a}(\mathbf{d}_h^k) \quad (3.24b)$$

$$\frac{1}{\epsilon} \mathbf{g}(\phi_h^{k+1}) + \epsilon \mathbf{E} \underline{\phi}^{k+1} + \mathbf{M}_{pf} \underline{\boldsymbol{\mu}}^{k+1} = \mathbf{0} \quad (3.24c)$$

Second, we solve the orientation field equations (3.22), already using the phase field variables at the new time.

$$\mathbf{M}_{of} \underline{\mathbf{d}}^{k+1} + \Delta t \mathbf{B}(\mathbf{u}^k) \underline{\mathbf{d}}^{k+1} + \Delta t \frac{1}{\kappa} \mathbf{M}_{of} \underline{\mathbf{d}}^{\natural, k+1} = \mathbf{M}_{of} \underline{\mathbf{d}}^k \quad (3.25a)$$

$$\mathbf{M}_{of} \underline{\mathbf{d}}^{\natural, k+1} + \frac{c_1}{\operatorname{Pa}} \mathbf{C}(\phi_h^{k+1}) \underline{\mathbf{d}}^{k+1} - \frac{c_1}{\operatorname{Pa}} \mathbf{f}(\mathbf{d}_h^{k+1}) - \frac{1}{\operatorname{Pa}} \mathbf{E} \underline{\mathbf{d}}^{k+1} = \mathbf{0} \quad (3.25b)$$

Finally, we solve the Stokes equations (3.23) with the new phase field and orientation field variables.

$$\mathbf{A} \underline{\mathbf{u}}^{k+1} + \mathbf{B}^T \underline{\mathbf{p}}^{k+1} = \mathbf{a} \left( \phi_h^{k+1}, \phi_h^{\natural, k+1}, \mathbf{d}_h^{k+1}, \mathbf{d}_h^{\natural, k+1} \right) \quad (3.26a)$$

$$\mathbf{B} \underline{\mathbf{u}}^{k+1} = \mathbf{0} \quad (3.26b)$$

### 3.6. Solvers and preconditioners

For the nonlinear systems (3.24) and (3.25), we use a backtracking Newton scheme using the values from the last time step as an initial guess. The Jacobians needed for the Newton scheme could be inverted using direct linear solvers [37]. However, the Jacobians are large and sparse, and the variables from the last Newton iteration (or the last time step) make good initial guesses. In this setting, iterative linear solvers are usually both faster and less memory-intensive than direct solvers. To choose suitable iterative solvers, we will thus take a closer look at the Jacobians of the nonlinear systems.

### 3.6.1. Phase field

The Jacobian of the phase field system (3.24) has the form

$$\mathbf{J}_{pf}(\phi, \mu) = \begin{pmatrix} \mathbf{M}_{pf} - \Delta t \mathbf{B}(\mathbf{u}) & \Delta t \gamma \mathbf{E} & \mathbf{0} \\ \frac{1}{\text{Be} \cdot \epsilon^2} D_{\phi} \mathbf{f}(\phi, \mu) & \mathbf{M}_{pf} & \frac{1}{\text{Ca}} \mathbf{M}_{pf} + \frac{1}{\text{Be}} \mathbf{E} + \frac{1}{\text{Be} \cdot \epsilon^2} D_{\underline{\mu}} \mathbf{f}(\phi) \\ \epsilon \mathbf{E} + \frac{1}{\epsilon} D_{\phi} \mathbf{g}(\phi) & \mathbf{0} & \mathbf{M}_{pf} \end{pmatrix} \quad (3.27)$$

where

$$(D_{\phi} \mathbf{f})_{ij} = \int_X W'''(\phi) \mu \varphi_i \varphi_j \, dx = \int_X 6\phi \mu \varphi_i \varphi_j \, dx, \quad (3.28a)$$

$$(D_{\underline{\mu}} \mathbf{f})_{ij} = (D_{\phi} \mathbf{g})_{ij} = \int_X W''(\phi) \varphi_i \varphi_j \, dx = \int_X (3\phi^2 - 1) \varphi_i \varphi_j \, dx. \quad (3.28b)$$

Obviously,  $\mathbf{J}_{pf}$  is non-symmetric. The mass matrix  $\mathbf{M}_{pf}$  and the stiffness matrix  $\mathbf{E}$  can be computed once and for all before starting the timestepping (as long as the grid does not change). The matrix  $\mathbf{B}$  depends on the fluid velocity and thus has to be recomputed for each new time step (before starting the Newton iterations). The Jacobians of the nonlinear terms  $\mathbf{f}$  and  $\mathbf{g}$  have to be reassembled in each Newton iteration.

The convergence rate of iterative solvers usually depends on the condition number of the matrix. Thus, preconditioners can greatly speed up (or merely enable) the solution process. To select a preconditioner for the phase field jacobian (3.27), we first have a look at the scaling of the matrix blocks (cmp. [9]) which is approximately

$$\begin{pmatrix} h^2 - \Delta t |\mathbf{u}| h & \Delta t \gamma & 0 \\ \frac{|\phi| |\mu| h^2}{\text{Be} \cdot \epsilon^2} & h^2 & \frac{h^2}{\text{Ca}} + \frac{1}{\text{Be}} + \frac{|3\phi^2 - 1| h^2}{\text{Be} \cdot \epsilon^2} \\ \epsilon + \frac{|3\phi^2 - 1| h^2}{\epsilon} & 0 & h^2 \end{pmatrix}$$

If we assume that  $\Delta t$  is small (e.g.,  $O(h^2)$ ) and further assume that the fluid velocity is of order 1, we see that the  $\Delta t \mathbf{B}(\mathbf{u})$  term scales with  $h^3$  and can thus be neglected (for  $h$  small enough) compared to the mass matrix  $\mathbf{M}_{pf}$  which is of order  $h^2$ .

To guarantee a sufficient resolution of the interface region, the phase field parameter  $\epsilon$  (or the grid width  $h$ ) is usually chosen such that  $h \leq c\epsilon$  where  $c$  is a small integer [9]. We can thus assume that these two parameters scale similarly. Moreover,  $\phi$  should take on values between  $[-1, 1]$  and is in particular bounded. If we further assume that the capillary numbers  $\text{Be}$  and  $\text{Ca}$  are of order 1, we see that it is not clear that we can neglect the Jacobians of the nonlinear terms as they seem to scale similar to the other terms in their respective block. However, outside the interface region, we have  $\phi^2 \approx 1$  and  $\mu \approx 0$  and thus

$$D_{\phi} \mathbf{f} \approx \mathbf{0} \quad (3.29a)$$

$$D_{\underline{\mu}} \mathbf{f} = D_{\phi} \mathbf{g} \approx 2\mathbf{M}_{pf} \quad (3.29b)$$

are reasonable approximations. Taken together, we obtain the preconditioner

$$\hat{\mathbf{J}}_{pf} = \begin{pmatrix} \mathbf{M}_{pf} & \Delta t \gamma \mathbf{E} & \mathbf{0} \\ \mathbf{0} & \mathbf{M}_{pf} & \left(\frac{1}{\text{Ca}} + \frac{2}{\text{Be} \cdot \epsilon^2}\right) \mathbf{M}_{pf} + \frac{1}{\text{Be}} \mathbf{E} \\ \epsilon \mathbf{E} + \frac{2}{\epsilon} \mathbf{M}_{pf} & \mathbf{0} & \mathbf{M}_{pf} \end{pmatrix}. \quad (3.30)$$

By the arguments above it is not totally clear that this preconditioner sufficiently approximates the matrix entries corresponding to the interface region as the Jacobians of the nonlinear parts (which we omitted) might contribute significantly here. However, our numerical tests indicate that (3.30) is indeed a good preconditioner for (3.27) (see Section 5).

### 3.6.2. Orientation field

In each step of the Newton scheme, we have to invert the Jacobian

$$\mathbf{J}_{of}(\mathbf{d}) = \begin{pmatrix} \mathbf{M}_{of} + \Delta t \mathbf{B}(\mathbf{u}) & \frac{\Delta t}{\kappa} \mathbf{M}_{of} \\ \frac{c_1}{\text{Pa}} \mathbf{C}(\phi) - \frac{1}{\text{Pa}} \mathbf{E} - \frac{c_1}{\text{Pa}} D_{\underline{\mathbf{d}}} \mathbf{f}(\mathbf{d}) & \mathbf{M}_{of} \end{pmatrix} \quad (3.31)$$

where the Jacobian of the nonlinear term has the entries

$$\begin{aligned} (D_{\underline{\mathbf{d}}} \mathbf{f})_{ij} &= \int_X \frac{\partial(\mathbf{d} \cdot \mathbf{d})}{\partial d_j} (\mathbf{d} \cdot \boldsymbol{\varphi}_i) + (\mathbf{d} \cdot \mathbf{d}) \frac{\partial(\mathbf{d} \cdot \boldsymbol{\varphi}_i)}{\partial d_j} \, dx \\ &= \int_X 2(\mathbf{d} \cdot \boldsymbol{\varphi}_j)(\mathbf{d} \cdot \boldsymbol{\varphi}_i) + (\mathbf{d} \cdot \mathbf{d})(\boldsymbol{\varphi}_j \cdot \boldsymbol{\varphi}_i) \, dx \end{aligned} \quad (3.32)$$

We can invert (3.31) by a Schur complement-type solver. Introducing

$$\mathbf{G}(\phi, \mathbf{d}) = \frac{c_1}{\text{Pa}} \mathbf{C}(\phi) - \frac{1}{\text{Pa}} \mathbf{E} - \frac{c_1}{\text{Pa}} D_{\underline{\mathbf{d}}} \mathbf{f}(\mathbf{d}) \quad (3.33)$$

we factorize (3.31) as

$$\begin{pmatrix} \mathbf{M}_{of} + \Delta t \mathbf{B}(\mathbf{u}) & \frac{\Delta t}{\kappa} \mathbf{M}_{of} \\ \mathbf{G}(\phi, \mathbf{d}) & \mathbf{M}_{of} \end{pmatrix} = \begin{pmatrix} \mathbf{I} & \frac{\Delta t}{\kappa} \mathbf{I} \\ \mathbf{0} & \mathbf{I} \end{pmatrix} \begin{pmatrix} \mathbf{M}_{of} + \Delta t \mathbf{B}(\mathbf{u}) - \frac{\Delta t}{\kappa} \mathbf{G}(\phi, \mathbf{d}) & \mathbf{0} \\ \mathbf{0} & \mathbf{M}_{of} \end{pmatrix} \begin{pmatrix} \mathbf{I} & \mathbf{0} \\ \mathbf{M}_{of}^{-1} \mathbf{G}(\phi, \mathbf{d}) & \mathbf{I} \end{pmatrix}. \quad (3.34)$$

The inverse of  $\mathbf{J}_{of}$  thus is

$$\mathbf{J}_{of}^{-1} = \begin{pmatrix} \mathbf{I} & \mathbf{0} \\ -\mathbf{M}_{of}^{-1} \mathbf{G}(\phi, \mathbf{d}) & \mathbf{I} \end{pmatrix} \begin{pmatrix} (\mathbf{M}_{of} + \Delta t \mathbf{B}(\mathbf{u}) - \frac{\Delta t}{\kappa} \mathbf{G}(\phi, \mathbf{d}))^{-1} & \mathbf{0} \\ \mathbf{0} & \mathbf{M}_{of}^{-1} \end{pmatrix} \begin{pmatrix} \mathbf{I} & -\frac{\Delta t}{\kappa} \mathbf{I} \\ \mathbf{0} & \mathbf{I} \end{pmatrix} \quad (3.35)$$

Note that the Schur complement matrix does not contain any inverse matrices. As a consequence, it is a sparse matrix (as  $\mathbf{M}_{of}$ ,  $\mathbf{B}$ ,  $\mathbf{G}$  are sparse) and can easily be assembled explicitly which enables the use of direct solvers. However, we will see in Section 5 that iterative solvers are also a good option since they converge quickly even when used without preconditioner.

## 4. Model order reduction

The cell model we are considering depends on a multitude of parameters

$$\boldsymbol{\eta} := (\epsilon, \gamma, c_1, \kappa, \xi, \text{Be}, \text{Ca}, \text{Pa}, \text{Fa}) \in \mathbb{R}^9$$

we might want to vary. However, each new combination of parameters will require a full new simulation of the model, which will make extensive studies of the influence of the parameters or even the optimization of the parameters w.r.t. some quantities of interest prohibitively expensive. To mitigate this issue, we will in this section derive a low-rank reduced order model using reduced-basis techniques, which can be used as a high-quality surrogate for the original discrete model (3.24)–(3.26).

### 4.1. Definition of the reduced order model

To simplify notation, we first stack the coefficient vectors such that there is only one vector for the phase field, orientation field and Stokes coefficients, respectively.

$$\boldsymbol{\varphi}^k = \begin{pmatrix} \underline{\phi}^k \\ \underline{\phi}^{\mathfrak{h},k} \\ \underline{\boldsymbol{\mu}}^k \end{pmatrix} \in \mathbb{R}^{n_\varphi}, \quad \mathbf{o}^k = \begin{pmatrix} \underline{\mathbf{d}}^k \\ \underline{\mathbf{d}}^{\mathfrak{h},k} \end{pmatrix} \in \mathbb{R}^{n_o}, \quad \mathbf{s}^k = \begin{pmatrix} \underline{\mathbf{u}}^k \\ \underline{\mathbf{p}}^k \end{pmatrix} \in \mathbb{R}^{n_s}$$

Here, the length of the vectors is  $n_\varphi = 3n_h^p$ ,  $n_{\mathbf{o}} = 2(n_h^p)^d$  and  $n_{\mathbf{s}} = (n_{h,0}^{p+1})^d + n_h^p$  (compare Section 3.4). We then rewrite equations (3.24)–(3.26) from Section 3.5 in the following condensed residual form:

$$\mathbf{r}_\varphi(\varphi^{k+1}(\boldsymbol{\eta}), \varphi^k(\boldsymbol{\eta}), \mathbf{o}^k(\boldsymbol{\eta}), \mathbf{s}^k(\boldsymbol{\eta}); \boldsymbol{\eta}) = \mathbf{0}, \quad (4.1a)$$

$$\mathbf{r}_{\mathbf{o}}(\mathbf{o}^{k+1}(\boldsymbol{\eta}), \mathbf{o}^k(\boldsymbol{\eta}), \varphi^{k+1}(\boldsymbol{\eta}), \mathbf{s}^k(\boldsymbol{\eta}); \boldsymbol{\eta}) = \mathbf{0}, \quad (4.1b)$$

$$\mathbf{r}_{\mathbf{s}}(\mathbf{s}^{k+1}(\boldsymbol{\eta}), \varphi^{k+1}(\boldsymbol{\eta}), \mathbf{o}^{k+1}(\boldsymbol{\eta}); \boldsymbol{\eta}) = \mathbf{0}, \quad (4.1c)$$

$$\varphi^0(\boldsymbol{\eta}) = \begin{pmatrix} \phi^0 \\ \mathbf{0} \\ \mathbf{0} \end{pmatrix}, \quad \mathbf{o}^0(\boldsymbol{\eta}) = \begin{pmatrix} \mathbf{d}^0 \\ \mathbf{0} \end{pmatrix}, \quad \mathbf{s}^0(\boldsymbol{\eta}) = \begin{pmatrix} \mathbf{u}^0 \\ \mathbf{0} \end{pmatrix} \quad (4.1d)$$

where the initial values  $\phi^0, \mathbf{d}^0, \mathbf{u}^0$  for the coefficient vectors are obtained from the initial values (3.12e), (3.13e), (3.14h) by interpolation.

Assume that  $\boldsymbol{\eta} \in \mathcal{P} \subseteq \mathbb{R}^9$  for some parameter domain of interest  $\mathcal{P}$  we want to explore, and further assume that we are given low-rank matrices  $\mathbf{V}_\varphi \in \mathbb{R}^{n_\varphi \times N_\varphi}$ ,  $\mathbf{V}_{\mathbf{o}} \in \mathbb{R}^{n_{\mathbf{o}} \times N_{\mathbf{o}}}$ ,  $\mathbf{V}_{\mathbf{s}} \in \mathbb{R}^{n_{\mathbf{s}} \times N_{\mathbf{s}}}$  with orthonormal columns such that each  $\varphi^k(\boldsymbol{\eta}), \mathbf{o}^k(\boldsymbol{\eta}), \mathbf{s}^k(\boldsymbol{\eta})$  can be well-approximated within the column-spans of these matrices for all  $0 \leq k \leq K$  and  $\boldsymbol{\eta} \in \mathcal{P}$ . The construction of these basis matrices will be discussed in Section 4.2.2.

Our aim is to find vectors  $\bar{\varphi}^k(\boldsymbol{\eta}) \in \mathbb{R}^{N_\varphi}$ ,  $\bar{\mathbf{o}}^k(\boldsymbol{\eta}) \in \mathbb{R}^{N_{\mathbf{o}}}$  and  $\bar{\mathbf{s}}^k(\boldsymbol{\eta}) \in \mathbb{R}^{N_{\mathbf{s}}}$  such that

$$\varphi^k(\boldsymbol{\eta}) \approx \mathbf{V}_\varphi \cdot \bar{\varphi}^k(\boldsymbol{\eta}), \quad \mathbf{o}^k(\boldsymbol{\eta}) \approx \mathbf{V}_{\mathbf{o}} \cdot \bar{\mathbf{o}}^k(\boldsymbol{\eta}), \quad \mathbf{s}^k(\boldsymbol{\eta}) \approx \mathbf{V}_{\mathbf{s}} \cdot \bar{\mathbf{s}}^k(\boldsymbol{\eta}). \quad (4.2)$$

To determine the reduced states  $\bar{\varphi}^k(\boldsymbol{\eta}), \bar{\mathbf{o}}^k(\boldsymbol{\eta}), \bar{\mathbf{s}}^k(\boldsymbol{\eta})$  we use the original system equations (4.1). However, substituting (4.2) into (4.1) will lead to an over-determined system. To close the system and ensure its stability, we choose a residual-minimization approach and define the reduced states as the solutions of

$$\bar{\varphi}^{k+1} = \underset{\bar{\varphi} \in \mathbb{R}^{\dim V_\varphi}}{\operatorname{argmin}} \left\| \mathbf{r}_\varphi(\mathbf{V}_\varphi \cdot \bar{\varphi}, \mathbf{V}_\varphi \cdot \bar{\varphi}^k(\boldsymbol{\eta}), \mathbf{V}_{\mathbf{o}} \cdot \bar{\mathbf{o}}^k(\boldsymbol{\eta}), \mathbf{V}_{\mathbf{s}} \cdot \bar{\mathbf{s}}^k(\boldsymbol{\eta}); \boldsymbol{\eta}) \right\|, \quad (4.3a)$$

$$\bar{\mathbf{o}}^{k+1} = \underset{\bar{\mathbf{o}} \in \mathbb{R}^{\dim V_{\mathbf{o}}}}{\operatorname{argmin}} \left\| \mathbf{r}_{\mathbf{o}}(\mathbf{V}_{\mathbf{o}} \cdot \bar{\mathbf{o}}, \mathbf{V}_{\mathbf{o}} \cdot \bar{\mathbf{o}}^k(\boldsymbol{\eta}), \mathbf{V}_\varphi \cdot \bar{\varphi}^{k+1}(\boldsymbol{\eta}), \mathbf{V}_{\mathbf{s}} \cdot \bar{\mathbf{s}}^k(\boldsymbol{\eta}); \boldsymbol{\eta}) \right\|, \quad (4.3b)$$

$$\bar{\mathbf{s}}^{k+1} = \underset{\bar{\mathbf{s}} \in \mathbb{R}^{\dim V_{\mathbf{s}}}}{\operatorname{argmin}} \left\| \mathbf{r}_{\mathbf{s}}(\mathbf{V}_{\mathbf{s}} \cdot \bar{\mathbf{s}}, \mathbf{V}_\varphi \cdot \bar{\varphi}^{k+1}(\boldsymbol{\eta}), \mathbf{V}_{\mathbf{o}} \cdot \bar{\mathbf{o}}^{k+1}(\boldsymbol{\eta}); \boldsymbol{\eta}) \right\|. \quad (4.3c)$$

These systems of equations can be solved iteratively using the Gauss-Newton method. However, while the model is now formulated on low-dimensional spaces, the computation of the residuals and Jacobians still requires high-dimensional computations, which will severely limit the computational speedup gained by this formulation. Thus, we apply an additional reduction step by employing the discrete empirical interpolation method (DEIM) [13] to the residuals. To this end, assume we are given collateral bases  $\mathbf{C}_\varphi \in \mathbb{R}^{n_\varphi \times M_\varphi}$ ,  $\mathbf{C}_{\mathbf{o}} \in \mathbb{R}^{n_{\mathbf{o}} \times M_{\mathbf{o}}}$  and  $\mathbf{C}_{\mathbf{s}} \in \mathbb{R}^{n_{\mathbf{s}} \times M_{\mathbf{s}}}$  of dimensions  $M_\varphi, M_{\mathbf{o}}, M_{\mathbf{s}}$  and matrices  $\mathbf{Z}_\varphi = [\mathbf{e}_{d_{\varphi,1}}, \dots, \mathbf{e}_{d_{\varphi,M_\varphi}}] \in \mathbb{R}^{M_\varphi \times M_\varphi}$ ,  $\mathbf{Z}_{\mathbf{o}} = [\mathbf{e}_{d_{\mathbf{o},1}}, \dots, \mathbf{e}_{d_{\mathbf{o},M_{\mathbf{o}}}}] \in \mathbb{R}^{M_{\mathbf{o}} \times M_{\mathbf{o}}}$  and  $\mathbf{Z}_{\mathbf{s}} = [\mathbf{e}_{d_{\mathbf{s},1}}, \dots, \mathbf{e}_{d_{\mathbf{s},M_{\mathbf{s}}}}] \in \mathbb{R}^{M_{\mathbf{s}} \times M_{\mathbf{s}}}$ , where  $1 \leq d_{\varphi,i} \leq n_\varphi$  ( $1 \leq i \leq M_\varphi$ ),  $1 \leq d_{\mathbf{o},i} \leq n_{\mathbf{o}}$  ( $1 \leq i \leq M_{\mathbf{o}}$ ) and  $1 \leq d_{\mathbf{s},i} \leq n_{\mathbf{s}}$  ( $1 \leq i \leq M_{\mathbf{s}}$ ) are pairwise disjoint sets of indices and (by abuse of notation)  $\mathbf{e}_i$  denotes the  $i$ -th canonical basis vector in the Euclidean space of appropriate dimension. Thus, for instance, left-multiplying  $\mathbf{r}_\varphi$  with  $\mathbf{Z}_\varphi^T$  extracts the  $M_\varphi$  DOFs of  $\mathbf{r}_\varphi$  with indices  $d_{\varphi,1}, \dots, d_{\varphi,M_\varphi}$ , and  $\mathbf{C}_\varphi(\mathbf{Z}_\varphi^T \mathbf{C}_\varphi)^{-1} \mathbf{Z}_\varphi^T \mathbf{r}_\varphi$  is the interpolation of  $\mathbf{r}_\varphi$  within the column span of  $\mathbf{C}_\varphi$  that agrees with  $\mathbf{r}_\varphi$  at all  $M_\varphi$  interpolation DOFs. The computation of the interpolation bases and DOFs is again covered in Section 4.2.

Replacing all residuals with their respective empirical interpolants leads us to the following hyper-reduced residual-minimization problem, that we will use as surrogate for the full-order model:

$$\bar{\varphi}^{k+1} = \operatorname{argmin}_{\bar{\varphi} \in \mathbb{R}^{\dim V_\varphi}} \left\| \mathbf{C}_\varphi (\mathbf{Z}_\varphi^T \mathbf{C}_\varphi)^{-1} \mathbf{Z}_\varphi^T \mathbf{r}_\varphi (\mathbf{V}_\varphi \cdot \bar{\varphi}, \mathbf{V}_\varphi \cdot \bar{\varphi}^k(\boldsymbol{\eta}), \mathbf{V}_\mathbf{o} \cdot \bar{\mathbf{o}}^k(\boldsymbol{\eta}), \mathbf{V}_\mathbf{s} \cdot \bar{\mathbf{s}}^k(\boldsymbol{\eta}); \boldsymbol{\eta}) \right\|, \quad (4.4a)$$

$$\bar{\mathbf{o}}^{k+1} = \operatorname{argmin}_{\bar{\mathbf{o}} \in \mathbb{R}^{\dim V_\mathbf{o}}} \left\| \mathbf{C}_\mathbf{o} (\mathbf{Z}_\mathbf{o}^T \mathbf{C}_\mathbf{o})^{-1} \mathbf{Z}_\mathbf{o}^T \mathbf{r}_\mathbf{o} (\mathbf{V}_\mathbf{o} \cdot \bar{\mathbf{o}}, \mathbf{V}_\mathbf{o} \cdot \bar{\mathbf{o}}^k(\boldsymbol{\eta}), \mathbf{V}_\varphi \cdot \bar{\varphi}^{k+1}(\boldsymbol{\eta}), \mathbf{V}_\mathbf{s} \cdot \bar{\mathbf{s}}^k(\boldsymbol{\eta}); \boldsymbol{\eta}) \right\|, \quad (4.4b)$$

$$\bar{\mathbf{s}}^{k+1} = \operatorname{argmin}_{\bar{\mathbf{s}} \in \mathbb{R}^{\dim V_\mathbf{s}}} \left\| \mathbf{C}_\mathbf{s} (\mathbf{Z}_\mathbf{s}^T \mathbf{C}_\mathbf{s})^{-1} \mathbf{Z}_\mathbf{s}^T \mathbf{r}_\mathbf{s} (\mathbf{V}_\mathbf{s} \cdot \bar{\mathbf{s}}, \mathbf{V}_\varphi \cdot \bar{\varphi}^{k+1}(\boldsymbol{\eta}), \mathbf{V}_\mathbf{o} \cdot \bar{\mathbf{o}}^{k+1}(\boldsymbol{\eta}); \boldsymbol{\eta}) \right\|. \quad (4.4c)$$

Thanks to the locality of all involved finite-element operators, the restricted residuals  $\mathbf{Z}_\varphi^T \mathbf{r}_\varphi$ ,  $\mathbf{Z}_\mathbf{o}^T \mathbf{r}_\mathbf{o}$ ,  $\mathbf{Z}_\mathbf{s}^T \mathbf{r}_\mathbf{s}$  and their Jacobians can be evaluated by only local computations in fixed-size neighborhoods of the interpolation DOFs. By storing the values of  $\mathbf{V}_\varphi$ ,  $\mathbf{V}_\mathbf{o}$ ,  $\mathbf{V}_\mathbf{s}$  at the DOFs of these neighborhoods, (4.4) can be solved with an effort that scales in space and time only with the reduced dimensions  $N_\varphi, N_\mathbf{o}, N_\mathbf{s}, M_\varphi, M_\mathbf{o}, M_\mathbf{s}$  and is independent of the dimensions of the finite-element spaces.

**Remark 4.1.** *While the Stokes residual is affine linear in  $\mathbf{s}$ , it nonlinearly depends on  $\varphi$  and  $\mathbf{o}$ . Hence, some form of hyper-reduction is also required for solving (4.3c). For ease of implementation, we chose here the same monolithic interpolation approach as for  $\mathbf{r}_\varphi$  and  $\mathbf{r}_\mathbf{o}$ . The Gauss-Newton algorithm will converge after one iteration when applied to (4.4c).*

#### 4.2. Distributed construction of approximation spaces

The approximation quality of (4.4) is strongly dependent on the choice of the reduced bases  $\mathbf{V}_\varphi$ ,  $\mathbf{V}_\mathbf{o}$ ,  $\mathbf{V}_\mathbf{s}$ ,  $\mathbf{C}_\varphi$ ,  $\mathbf{C}_\mathbf{o}$ ,  $\mathbf{C}_\mathbf{s}$ . In the following, we will outline the construction of these reduced bases using the hierarchical approximate proper orthogonal decomposition (HAPOD) [28]. To that end, we shortly recall the proper orthogonal decomposition (POD).

##### 4.2.1. POD

The proper orthogonal decomposition (POD) builds low-rank approximation spaces for the column vectors of a given matrix of solution snapshots  $\mathbf{S} \in \mathbb{R}^{n \times s}$  from the left-singular vectors corresponding to the dominant singular values of  $\mathbf{S}$ . We consider here the weighted version, where the singular value decomposition (SVD) is computed by interpreting  $\mathbf{S}$  as a linear operator on the finite-dimensional Hilbert space  $(\mathbb{R}^n, \mathbf{W})$ , where the symmetric positive matrix  $\mathbf{W} \in \mathbb{R}^{n \times n}$  induces the inner product and norm

$$(\mathbf{y}_1, \mathbf{y}_2)_W := \mathbf{y}_1^T \mathbf{W} \mathbf{y}_2 \quad \text{and} \quad \|\mathbf{y}_1\|_W := \sqrt{(\mathbf{y}_1, \mathbf{y}_1)_W}. \quad (4.5)$$

Using the so-called *method of snapshots* [50] to determine the SVD of  $\mathbf{S}$  via an eigendecomposition of the associated weighted Gramian  $\mathbf{S}^T \cdot \mathbf{W} \cdot \mathbf{S} \in \mathbb{R}^{s \times s}$  yields the following algorithm:

---

**Algorithm 1:** POD( $\mathbf{S}$ ,  $\mathbf{W}$ ,  $\varepsilon$ ): weighted POD via method of snapshots

---

**input** : snapshot matrix  $\mathbf{S} \in \mathbb{R}^{n \times s}$ , inner product matrix  $\mathbf{W} \in \mathbb{R}^{n \times n}$ , error tolerance  $\varepsilon > 0$   
**output**: POD modes  $\mathbf{U} \in \mathbb{R}^{n \times N}$ , singular values  $\boldsymbol{\sigma}$

- 1  $\mathbf{G} := \mathbf{S}^T \cdot \mathbf{W} \cdot \mathbf{S}$ ; // weighted  $s \times s$  Gramian matrix
- 2  $\boldsymbol{\lambda}, \mathbf{V} := \operatorname{eigh}(\mathbf{G})$ ; //  $\lambda_i, \mathbf{V}_{:,i} = i$ -th eigen-value/-vector ordered by magnitude
- 3  $N := \min\{M \in \mathbb{N}^{\geq 0} \mid \sum_{i=M+1}^s \lambda_i^2 \leq \varepsilon\}$ ;
- 4  $\boldsymbol{\lambda}_\varepsilon, \mathbf{V}_\varepsilon := \boldsymbol{\lambda}(1 : N), \mathbf{V}(:, 1 : N)$ ; // truncate according to given tolerance
- 5  $\boldsymbol{\sigma} := \sqrt{\boldsymbol{\lambda}_\varepsilon}$ ; // singular values
- 6  $\mathbf{U} := \mathbf{S} \cdot \mathbf{V}_\varepsilon \cdot \operatorname{diag}(\boldsymbol{\sigma})^{-1}$ ; // left-singular vectors

---

By definition of the SVD, the POD modes  $\mathbf{U}$  are  $\mathbf{W}$ -orthonormal, i.e.  $\mathbf{U}^T \mathbf{W} \mathbf{U} = \mathbf{I}$ . In particular, the  $\mathbf{W}$ -orthonormal projection  $P_{\operatorname{colspan} \mathbf{U}}$  onto the approximation space spanned by the POD modes is given by

the formula

$$P_{\text{colspan } \mathbf{U}}(\mathbf{y}) = \mathbf{P}_{\mathbf{U}} \cdot \mathbf{y} := \mathbf{U}\mathbf{U}^T\mathbf{W}\mathbf{y}. \quad (4.6)$$

The main reason for the importance of the POD is the fact that it produces best approximating spaces for the snapshot data in the  $\ell^2$ -sense:

**Theorem 4.2** (Schmidt-Eckhard-Young-Mirsky). *Let  $\mathbf{U}, \boldsymbol{\sigma} := \text{POD}(\mathbf{S}, \mathbf{W}, \varepsilon)$  be the POD modes and singular values for a given snapshot matrix  $\mathbf{S}$ , inner product matrix  $\mathbf{W}$  and truncation tolerance  $\varepsilon$ . Then  $\text{colspan } \mathbf{U}$  is an  $\ell^2$ -best approximating space for  $\mathbf{S}$  in the sense that*

$$\sum_{i=1}^s \|\mathbf{S}_{:,i} - P_{\text{colspan } \mathbf{U}}(\mathbf{S}_{:,i})\|_{\mathbf{W}}^2 = \min_{\substack{V \subseteq \mathbb{R}^n \\ \text{lin. subsp.} \\ \dim V = N}} \sum_{i=1}^s \|\mathbf{S}_{:,i} - P_V(\mathbf{S}_{:,i})\|_{\mathbf{W}}^2 = \sum_{i=N+1}^s \lambda_i \leq \varepsilon^2, \quad (4.7)$$

where  $\boldsymbol{\lambda}$  denotes the vector of untruncated squared singular values as in the definition of Algorithm 1. The dimension of the POD space  $N$  is the minimal dimension for which the  $\ell^2$  error is not larger than the given tolerance  $\varepsilon$ .

**Remark 4.3.** *We note that we could have equally well used any other approach for the computation of the SVD in Algorithm 1, e.g. QR decomposition or a randomized method. We choose the method of snapshots here, as it is particularly easy to implement efficiently for small  $s$ , which is the case when it is used as part of the HAPOD algorithms introduced in the following section.*

#### 4.2.2. HAPOD

Directly computing the POD for large snapshot sets can be computationally demanding. This is, in particular, the case, when the snapshot data grows so large that it not longer fits into memory. The Hierarchical Approximate POD (HAPOD) introduced in [28] is a flexible approach to partition the problem of computing the POD of a large dataset into smaller subproblems, which, depending on the structure of the computational setup, can be either solved incrementally or in parallel. Each of these subproblems consists in computing a POD of a small subset of the snapshot data in combination with POD modes from previous subproblems. The resulting local POD modes are then scaled by their singular values and sent to the next node in the computation.

To formalize this procedure, we consider rooted trees where to each node of the tree a local POD is associated. A rooted tree is a connected acyclic graph  $\mathcal{T}$  with nodes  $\mathcal{N}_{\mathcal{T}}$  of which  $\rho_{\mathcal{T}} \in \mathcal{N}_{\mathcal{T}}$  is designated as the root of the tree. For each node  $\alpha \in \mathcal{N}_{\mathcal{T}}$ , we denote by  $\mathcal{C}_{\mathcal{T}}(\alpha) \subset \mathcal{N}_{\mathcal{T}}$  the children of  $\alpha$ , i.e., all nodes connected to  $\alpha$  which cannot be reached from  $\rho_{\mathcal{T}}$  without first visiting  $\alpha$ . By  $\mathcal{L}_{\mathcal{T}} := \{\alpha \in \mathcal{N}_{\mathcal{T}} \mid \mathcal{C}_{\mathcal{T}}(\alpha) = \emptyset\}$  we denote the leafs of  $\mathcal{T}$ , i.e., the nodes which do not have any children.

To define the HAPOD, let a snapshot matrix  $\mathbf{S}$  and an inner product matrix  $\mathbf{W}$  be given. For a given tree  $\mathcal{T}$ , assign to each leaf  $\gamma \in \mathcal{L}_{\mathcal{T}}$  a set of column indices  $D(\gamma) \subseteq \{1, \dots, s\}$  s.t.  $D(\gamma_1) \cap D(\gamma_2) = \emptyset$  for different leafs  $\gamma_1 \neq \gamma_2$  and s.t.  $\bigcup_{\gamma \in \mathcal{L}_{\mathcal{T}}} D(\gamma) = \{1, \dots, s\}$ . By  $\mathbf{S}_{D(\gamma)}$  we then denote the  $n \times |D(\gamma)|$  matrix given by

$$\mathbf{S}_{D(\gamma)} := [\mathbf{S}_{:,D(\gamma)_1} \cdots \mathbf{S}_{:,D(\gamma)_{|D(\gamma)|}}],$$

where  $D(\gamma)_1, \dots, D(\gamma)_{|D(\gamma)|}$  is an arbitrary enumeration of  $D(\gamma)$ . Thus all snapshot vectors of  $\mathbf{S}$  are contained in exactly one local snapshot matrix  $\mathbf{S}_{D(\gamma)}$ . Further choosing local POD tolerances  $\varepsilon(\alpha) \in \mathbb{R}^{\geq 0}$  for

each node  $\alpha \in \mathcal{N}_{\mathcal{T}}$ , we can recursively define:

---

**Algorithm 2:** HAPOD[ $\mathbf{S}, \mathbf{W}, \mathcal{T}, D, \varepsilon$ ]( $\alpha$ ): local HAPOD at node  $\alpha \in \mathcal{N}_{\mathcal{T}}$

---

**input** : snapshot matrix  $\mathbf{S} \in \mathbb{R}^{n \times s}$ , inner product matrix  $\mathbf{W} \in \mathbb{R}^{n \times n}$ , snapshot distribution  $D$ , error tolerances  $\varepsilon$ , node  $\alpha$

**output:** scaled HAPOD modes  $\mathbf{U}_{\alpha} \in \mathbb{R}^{n \times N}$

```

1 if  $\alpha \in \mathcal{L}_{\mathcal{T}}$  then
2   |  $\mathbf{S}_{\alpha} := \mathbf{S}_{D(\alpha)}$ ;
3 else
4   |  $\mathbf{S}_{\alpha} := [\text{HAPOD}[\mathbf{S}, \mathbf{W}, \mathcal{T}, D, \varepsilon](\mathcal{C}_{\mathcal{T}}(\alpha)_1) \cdots \text{HAPOD}[\mathbf{S}, \mathbf{W}, \mathcal{T}, D, \varepsilon](\mathcal{C}_{\mathcal{T}}(\alpha)_{|\mathcal{C}_{\mathcal{T}}(\alpha)|})]$ ;
5 end
6 if  $\varepsilon(\alpha) = 0$  then
7   |  $\mathbf{U}_{\alpha}, \boldsymbol{\sigma}_{\alpha} := \mathbf{S}_{\alpha}, [1 \cdots 1]$ ; // No POD when tolerance is 0.
8 else
9   |  $\mathbf{U}_{\alpha}, \boldsymbol{\sigma}_{\alpha} := \text{POD}(\mathbf{S}_{\alpha}, \mathbf{W}, \varepsilon(\alpha))$ ;
10 end
11 if  $\alpha \neq \rho_{\mathcal{T}}$  then
12   |  $\mathbf{U}_{\alpha} := \mathbf{U}_{\alpha} \cdot \text{diag } \boldsymbol{\sigma}_{\alpha}$ ; // Scale POD modes when not at root.
13 end

```

---

In this definition,  $\mathcal{C}_{\mathcal{T}}(\alpha)_i$  again denotes an arbitrary enumeration of  $\mathcal{C}_{\mathcal{T}}(\alpha)$ . We note that the special case for  $\varepsilon(\alpha) = 0$  is included in the algorithm to allow incremental POD computations where new snapshot data directly enters a POD with the current modes, without first applying a POD only to the new data. The hierarchical approximate POD is now simply given by the local POD modes at the root node:

$$\text{HAPOD}[\mathbf{S}, \mathbf{W}, \mathcal{T}, D, \varepsilon] := \text{HAPOD}[\mathbf{S}, \mathbf{W}, \mathcal{T}, D, \varepsilon](\rho_{\mathcal{T}}).$$

If the local POD tolerances are chosen as [28]

$$\varepsilon(\alpha) = \begin{cases} \sqrt{|\mathcal{S}|} \cdot \omega \cdot \varepsilon^* & \text{if } \alpha = \rho_{\mathcal{T}} \\ \sqrt{|\tilde{\mathcal{S}}_{\alpha}|} \cdot (L_{\mathcal{T}} - 1)^{-1/2} \cdot \sqrt{1 - \omega^2} \cdot \varepsilon^* & \text{else,} \end{cases} \quad (4.8)$$

then the mean  $\ell^2$  projection error is bounded by  $\varepsilon^*$ , i.e.

$$\left( \frac{1}{|\mathcal{S}|} \sum_{\mathbf{v} \in \mathcal{S}} \|\mathbf{v} - P_{\text{colspan } \mathbf{U}}(\mathbf{v})\|_{\mathbf{W}}^2 \right)^{\frac{1}{2}} \leq \varepsilon^*. \quad (4.9)$$

Here, the parameter  $0 \leq \omega \leq 1$  can be chosen arbitrarily and allows to find the best compromise between efficiency of the HAPOD and the optimality of the resulting approximation space.

#### 4.2.3. Application of HAPOD-DEIM to our model

We now want to use the HAPOD to construct the reduced bases  $\mathbf{V}_{\varphi}, \mathbf{V}_{\mathbf{o}}, \mathbf{V}_{\mathbf{s}}, \mathbf{C}_{\varphi}, \mathbf{C}_{\mathbf{o}}, \mathbf{C}_{\mathbf{s}}$  for our model.

To that end, we first choose symmetric positive definite weight matrices  $\mathbf{W}_{\varphi}, \mathbf{W}_{\mathbf{o}}$  and  $\mathbf{W}_{\mathbf{s}}$  which, by (4.5), define inner products such that the coefficient spaces  $W_{\varphi} = (\mathbb{R}^{n_{\varphi}}, (\cdot, \cdot)_{W_{\varphi}})$ ,  $W_{\mathbf{o}} = (\mathbb{R}^{n_{\mathbf{o}}}, (\cdot, \cdot)_{W_{\mathbf{o}}})$  and  $W_{\mathbf{s}} = (\mathbb{R}^{n_{\mathbf{s}}}, (\cdot, \cdot)_{W_{\mathbf{s}}})$  are Hilbert spaces.

If we choose the weight matrices as the unit matrices, we obtain the standard Euclidean inner products. On the other hand, if we use the mass matrices  $\mathbf{M}_{pf}, \mathbf{M}_{of}, \mathbf{M}_{st}$  of the finite element discretization's basis functions, the resulting inner product is the  $L^2$  inner product of the finite element approximation functions.

Now, to compute the reduced bases, we would like to solve the high-dimensional problem (4.1) for all parameters in a training parameter set

$$\mathcal{P}_{train} = \{\boldsymbol{\eta}_m \mid m \in \{0, \dots, n_{train} - 1\}\},$$

which is assumed to be representative for the set of parameters, and then perform a POD for each of the snapshot multisets obtained by collecting the computed vectors and residuals:

$$\mathcal{S}_\alpha = \{\boldsymbol{\alpha}^k(\boldsymbol{\eta}_m) \in W_\alpha \mid k \in \{0, \dots, K\}, m \in \{0, \dots, n_{train} - 1\}\} \quad (4.10a)$$

$$\mathcal{R}_\alpha = \{\mathbf{r}_\alpha^{k,r}(\boldsymbol{\eta}_m) \in W_\alpha \mid k \in \{0, \dots, K - 1\}, m \in \{0, \dots, n_{train} - 1\}, r \in \{0, \dots, n_{it,\alpha}^k - 1\}\} \quad (4.10b)$$

for  $\alpha \in \{\boldsymbol{\varphi}, \mathbf{o}, \mathbf{s}\}$  where  $n_{it,\boldsymbol{\varphi}}^k, n_{it,\mathbf{o}}^k, n_{it,\mathbf{s}}^k$  are the number of iterations in the Newton scheme for the respective field in the  $k$ -th time step and

$$\begin{aligned} \mathbf{r}_\varphi^{k,r}(\boldsymbol{\eta}_m) &= \mathbf{r}_\varphi(\boldsymbol{\varphi}^{k,r}(\boldsymbol{\eta}_m), \boldsymbol{\varphi}^k(\boldsymbol{\eta}_m), \mathbf{o}^k(\boldsymbol{\eta}_m), \mathbf{s}^k(\boldsymbol{\eta}_m); \boldsymbol{\eta}_m) \\ \mathbf{r}_\mathbf{o}^{k,r}(\boldsymbol{\eta}_m) &= \mathbf{r}_\mathbf{o}(\mathbf{o}^{k,r}(\boldsymbol{\eta}_m), \boldsymbol{\varphi}^{k+1}(\boldsymbol{\eta}_m), \mathbf{o}^k(\boldsymbol{\eta}_m), \mathbf{s}^k(\boldsymbol{\eta}_m); \boldsymbol{\eta}_m) \\ \mathbf{r}_\mathbf{s}^{k,r}(\boldsymbol{\eta}_m) &= \mathbf{r}_\mathbf{s}(\mathbf{s}^{k,r}(\boldsymbol{\eta}_m), \boldsymbol{\varphi}^{k+1}(\boldsymbol{\eta}_m), \mathbf{o}^{k+1}(\boldsymbol{\eta}_m); \boldsymbol{\eta}_m) \end{aligned}$$

with  $\boldsymbol{\alpha}^{k,r}$  the  $r$ -th iterate in the Newton scheme for field  $\alpha$  in time step  $k$ . Note that, since the Stokes residual is affine linear in  $\mathbf{s}$ , we have  $n_{it,\mathbf{s}}^k = 1$ .

We could then perform a POD for each of the snapshot sets to obtain our reduced basis. However, since we have relatively small time steps  $\Delta t$  and since we often have to use hundreds of training parameters to get a good approximation of the parameter space, the snapshot sets (4.10) will be very large. As a consequence, directly computing the PODs for the snapshot sets, for example via the method of snapshots (see Algorithm 1), will take a very long time or even be practically impossible. We will thus apply the HAPOD to obtain an approximate POD decomposition with much less computing effort. Instead of computing the whole snapshot sets (4.10) at a time, which might exceed the available memory and require input/output operations to a mass storage device, for the HAPOD we choose a chunk size  $l$  and only compute  $l$  time steps at a time, obtaining the much smaller multisets

$$\mathcal{S}_{\alpha,a}(\boldsymbol{\eta}_m) = \{\boldsymbol{\alpha}^k(\boldsymbol{\eta}_m) \in W_\alpha \mid k \in \{a \cdot l, \dots, \min((a+1) \cdot l, K)\}\} \quad (4.11a)$$

$$\mathcal{R}_{\alpha,a}(\boldsymbol{\eta}_m) = \{\mathbf{r}_\alpha^{k,r}(\boldsymbol{\eta}_m) \in W_\alpha \mid k \in \{a \cdot l, \dots, \min((a+1) \cdot l, K)\}\} \quad (4.11b)$$

for  $m \in \{0, \dots, n_{train} - 1\}$  and  $\alpha \in \{\boldsymbol{\varphi}, \mathbf{o}, \mathbf{s}\}$ . We then already compute a local POD for each of these multisets separately, then scale the resulting modes by their corresponding singular values, and collect these scaled modes to perform another POD on the main rank of the compute node. Only then we compute the next chunk of time steps and again perform a local POD and a POD with the collected modes. This time, in the second POD with the collected modes, we also include the scaled modes from the last timesteps. We proceed like this until we computed all chunks of time steps. If we use several compute nodes, we then perform a final POD with the collected output modes from all compute nodes. The whole algorithm can be found in Algorithm 3.

## 5. Numerical experiments

### 5.1. Numerical solvers

Before turning to the model order reduction, we first validate the choice of our numerical solvers for the high-dimensional problem (see Section 3.6). As a test case, we use an initially circular cell in the domain  $X = [0, 30]^2$  with microtubules aligned across the  $x$ -direction, i.e.

$$\phi_0(\mathbf{x}) = \tanh\left(\frac{r(\mathbf{x})}{\sqrt{2}\epsilon}\right), \quad \mathbf{d}_0(\mathbf{x}) = \begin{pmatrix} 1 \\ 0 \end{pmatrix} \cdot \frac{\phi_0(\mathbf{x}) + 1}{2}, \quad \mathbf{u}_0(\mathbf{x}) = \mathbf{0}$$

---

**Algorithm 3:** HAPOD applied to cell model

---

```
1 function get_local_tolerance( $\varepsilon^*$ ,  $L_{\mathcal{T}}$ , num_snaps_in_leafs, is_root_node):
2   if is_root_node then
3     return  $\varepsilon^* \cdot \omega \cdot \sqrt{\text{num\_snaps\_in\_leafs}}$ 
4   else
5     return  $\varepsilon^* \cdot \sqrt{(1 - \omega^2) \frac{\text{num\_snaps\_in\_leafs}}{L_{\mathcal{T}} - 1}}$ 
6   end
7
8 function main(...):
9    $\eta \leftarrow$  distribute_parameters(...) // For simplicity, assume one parameter  $\eta$  per rank
10   $K = \lceil \frac{t_f}{\Delta t} \rceil$  // number of time steps
11   $n_{\text{chunks}} = \lceil \frac{K+1}{l} \rceil$  //  $K+1$  to include initial values
12  input_for_node_level_POD  $\leftarrow$  [[], [], [], [], [], []] // List of 6 empty lists
13  num_snaps_in_leafs  $\leftarrow$  [0, 0, 0, 0, 0, 0]
14  for  $a \leftarrow 0$  to  $n_{\text{chunks}} - 1$  do
15    Compute next  $l$  time steps according to (3.24)–(3.26) ( $l - 1$  for first,  $l_{\text{last}}$  for last chunk)
16    for  $i, \mathcal{S}_a$  in enumerate( $\mathcal{S}_{\varphi,a}(\eta)$ ,  $\mathcal{S}_{o,a}(\eta)$ ,  $\mathcal{S}_{s,a}(\eta)$ ,  $\mathcal{R}_{\varphi,a}(\eta)$ ,  $\mathcal{R}_{o,a}(\eta)$ ,  $\mathcal{R}_{s,a}(\eta)$ ) do
17      // Perform a POD for the local snapshots on each MPI rank
18       $\varepsilon \leftarrow$  get_local_tolerance( $\varepsilon^*$ ,  $L_{\mathcal{T}}$ ,  $|\mathcal{S}_a|$ , false)
19      modes, singular_values  $\leftarrow$  POD( $\mathcal{S}_a, \varepsilon$ )
20      modes *= singular_values // Scale vectors in modes by their corresponding
21      singular value
22      // Now collect the modes on the main MPI rank on each compute node.
23      // Instead of using MPI rank 0 for all  $i$ , we could also use
24      // rank  $i$  to perform the PODs on node level in parallel for all 6 fields.
25      collected_modes  $\leftarrow$  // Gathered vectors from all modes variables
26      num_snaps  $\leftarrow$  // Sum of  $|\mathcal{S}_a|$  over all MPI ranks on node
27      if node_rank = 0 then
28        num_snaps_in_leafs[ $i$ ] += num_snaps
29         $\varepsilon =$  get_local_tolerance( $\varepsilon^*$ ,  $L_{\mathcal{T}}$ , num_snaps_in_leafs[ $i$ ], false)
30        input_for_node_level_POD[ $i$ ].append(collected_modes)
31        modes, singular_values  $\leftarrow$  POD(input_for_node_level_POD[ $i$ ],  $\varepsilon$ )
32        input_for_node_level_POD[ $i$ ] = modes * singular_values
33      end
34    end
35  end
36  // Now perform the final POD using the collected inputs from all compute nodes.
37  // For simplicity, we perform a single POD here. In our actual implementation,
38  // we again apply a HAPOD over a binary tree of compute nodes.
39  bases  $\leftarrow$  [None, None, None, None, None, None]
40  for  $i \leftarrow 0$  to 5 do
41    collected_inputs  $\leftarrow$  // Gathered vectors from all input_for_node_level_POD[ $i$ ]
42    variables
43    num_snaps  $\leftarrow$  // Sum of num_snaps_in_leafs[ $i$ ] over all compute nodes
44    if world_rank = 0 then
45       $\varepsilon =$  get_local_tolerance( $\varepsilon^*$ ,  $L_{\mathcal{T}}$ , num_snaps, true)
46      bases[ $i$ ], _  $\leftarrow$  POD(collected_inputs,  $\varepsilon$ )
47    end
48  end
49  end
```

---

where  $r$  is the signed distance function to the cell membrane ( $r(\mathbf{x}) = 5 - \left\| (15, 15)^T - \mathbf{x} \right\|$ ). To test the solvers, we compute the first 50 time steps of the first-order ( $p = 1$ ) finite element discretization from Section 3.4 for different grid sizes and different choices of the linear solvers. For all three systems, we use the UMFPACK [16] solver to directly invert the system matrix. For the phase field and orientation field jacobians, we also test an iterative GMRES solver which is taken from dune-istl [7] (`RestartedGMRESolver`) and used without preconditioner for the orientation field system. However, the GMRES solver does not converge in the phase field case. We thus use an incomplete LU factorization of the matrix (3.30) as a preconditioner (using `IncompleteLUT` from the Eigen package [23] with a fill factor of 80). For the orientation field and Stokes matrices, we also consider a Schur-complement approach (see Section 3.6.2 for the orientation field and, e.g., [6] for the Stokes system) coupled with an iterative solver. Here we use GMRES for the non-symmetric Schur complement of the orientation field jacobian and CG (dune-istl’s `CGSolver`) preconditioned with the pressure mass matrix [42] for the symmetric positive-definite Stokes Schur complement. All mass matrices needed in the Schur solvers or for the preconditioners are inverted using the sparse Cholesky factorization (`SimplicialLLDLT`) of the Eigen package. Since both the mass matrices and the preconditioner matrix (3.30) are time-independent, the (incomplete) factorization has to be performed only once before starting the time stepping. During the time-stepping, we can then efficiently apply the inverse matrix using this factorization.

The results can be found in Table 5.1 and are computed for a single fixed parameter value of  $Be = Ca = Pa = Fa = 1$ . However, we also tested several other parameters to make sure the results do not change significantly with the choice of parameter. The rows labelled *Setup* contain the time that is needed initially for setting up the solver before starting the timestepping. Almost all of this time is used for the initial factorization of the matrices. For the phase field and orientation field equations, which are nonlinear, the direct solvers cannot precompute any factorization and thus are set up very fast. However, the factorization then has to be done prior to each solve which is why the average time per matrix inversion (*Solve* rows of the table) is about an order of magnitude smaller for the iterative solvers, in particular for the finer grids. This holds true even for the orientation field system where the (unpreconditioned) GMRES solver on average needs over a hundred iterations to converge. Still, a preconditioner might be needed when refining the grid even further, as the iteration count increases with the grid size. Fortunately, the Schur complement seems to be well-conditioned even for the finer grids and has a very low cost per GMRES iteration as no matrix inversions are needed for its computation. As a consequence, it is again about an order of magnitude faster than the full-system GMRES solver. Memory-wise, the direct solver is much more demanding and uses about thrice as much memory as the two iterative solvers. If necessary, memory-usage of the iterative solvers could probably further be reduced by using iterative solvers also for the inversion of the mass matrices.

For the phase field matrices, preconditioning using the preconditioner (3.30) seems to work well in practice, though the iterations slowly increase when refining the grid. However, even on the finest grid tested, only about 14 iterations are needed for convergence, while the solver does not converge at all without preconditioning. The increase in the number of iterations might also be partly due to the fact that we use a fixed time step of  $\Delta t = 10^{-3}$  across all grid sizes such that the ratio of time step  $\Delta t$  to grid width  $h$  increases when refining the grid (remember that we assumed that  $\Delta t$  is small compared to  $h$  when deriving the preconditioner, see Section 3.6.1). Though significantly faster than the direct solver, the iterative solver is still the limiting factor for the overall solution process (remember that we have to invert the phase field jacobian once in each Newton iteration, while only once per timestep for the linear Stokes system). However, note that all measurements were done in serial computations. In principle, parallelization could be used both for the preconditioner and the GMRES solver to reduce computation times.

The Stokes system matrix is time-independent such that in this case also the direct solver has to perform only a single matrix factorization, which is why it is even a little faster than the iterative Schur complement CG solver. However, the difference is less than a factor of two, and the iterative solver uses significantly less memory, which is why we are using the iterative solver for the numerical experiments in this paper. Of course, there has been a lot of research on linear solvers for the Stokes system such that more advanced (and probably much faster) solvers would be available (see e.g., [6, 22]). However, as long as the phase field

solver limits overall solution time, the simple Schur-CG solver is sufficiently fast for our purposes.

In the following, we will always use the preconditioned GMRES solver for the phase field system, the unpreconditioned Schur-GMRES solver for the orientation field system and the Schur-CG solver preconditioned by the pressure mass matrix for the Stokes system.

## 5.2. Cell isolation experiment

As a first test for our numerical setup, we consider a cell isolation experiment as in [49]. A drosophila wing epithelial cell is isolated from the surrounding tissue by laser ablation (see Figure 5.1). Intriguingly, the ablation has almost no effect on the cell shape except for a small isotropic decrease in volume. The authors in [49] conclude that the epithelial cells are mostly force-autonomous during this developmental stage. They further show evidence that there is a balance between extensile forces generated by microtubules and the contractile forces of the actomyosin cortex.

To reproduce this setting, we consider a polygonal cell with vertices  $(10., 18.)^T$ ,  $(13., 13.)^T$ ,  $(19., 13.)^T$ ,  $(28.5, 16.)^T$ ,  $(25., 23.5)^T$ ,  $(15., 23.)^T$  in the domain  $X = [0, 40]^2$ . Let again  $r(\mathbf{x})$  be the signed distance of  $\mathbf{x}$  to the polygonal cell boundary such that  $r(\mathbf{x}) \geq 0$  if  $\mathbf{x}$  is inside the cell and  $r(\mathbf{x}) < 0$  for  $\mathbf{x}$  outside of the cell. We then choose the initial condition for the phase field as  $\phi_0 = \tanh\left(\frac{r(\mathbf{x})}{\sqrt{2}\epsilon}\right)$ . In addition, we assume that the microtubules are initially approximately aligned with the elongation of the cell, i.e.,  $\mathbf{d}_0 = (0.99, 0.14)^T$ , and that the fluid is at rest ( $\mathbf{u}_0 = \mathbf{0}$ ). Figure 5.2 shows the initial values and numerical solutions for two different parameter choices. As can be seen in the figure, for  $Ca = 1$ , the cell becomes elongated and there is still significant fluid flow visible at time  $t = 5$ . In contrast, for  $Ca = 0.2$ , the cell is almost in steady state at time  $t = 5$ . Moreover, the cell approximately maintains its shape except that it becomes rounded.

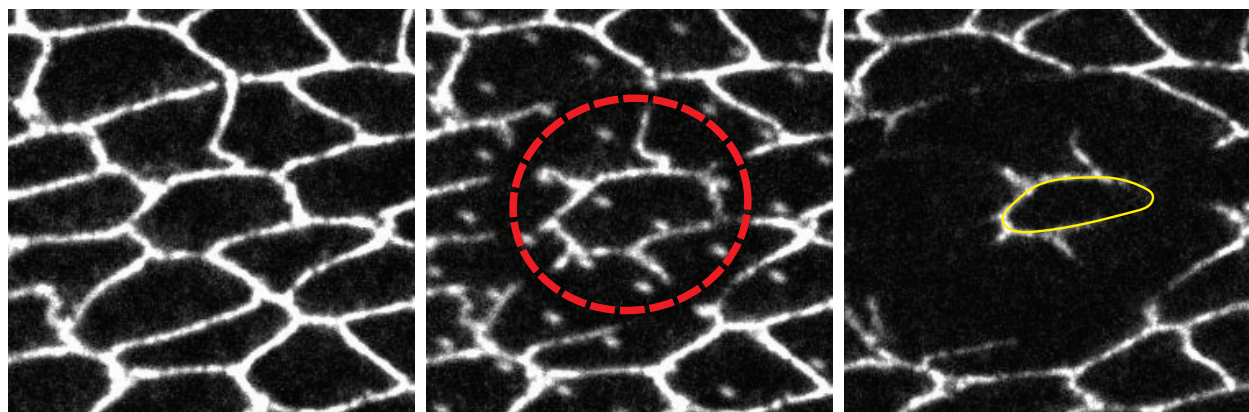


Figure 5.1: A drosophila wing epithelial cell is isolated from the surrounding tissue by laser ablation. The isolated cell mostly maintains its shape, the only change is a small isotropic decrease in cell size. This shows that at this stage (16h APF) of the wing development, cells are not shaped by their neighbors but mostly by cell-autonomous forces (see [49]).

## 5.3. Model order reduction

### 5.3.1. HAPOD-DEIM approximation of single fields

As described in Section 4, we build reduced bases separately for phase field, orientation field and the Stokes variables. However, since the equations are all coupled, errors in one of these fields will also influence the other fields, i.e., an approximation of the phase field variables will also result in errors in orientation field and Stokes variables and vice versa. In the worst case, these errors might even be amplified, e.g., a small error in the phase field might result in large errors in the orientation field. To test whether this is the case, we first reduce only one field at a time and analyse the errors that are introduced in all fields.

| Elements |           | Phase field solver |       | Orientation field solver |       |             | Stokes solver |          |
|----------|-----------|--------------------|-------|--------------------------|-------|-------------|---------------|----------|
|          |           | Direct             | GMRES | Direct                   | GMRES | Schur-GMRES | Direct        | Schur-CG |
| 3,600    | It.       | —                  | 7     | —                        | 65    | 33          | —             | 21       |
|          | Setup [s] | 0.1                | 1.0   | 0.2                      | 0.2   | 0.1         | 0.5           | 0.1      |
|          | Solve [s] | 0.6                | 0.1   | 1.1                      | 0.3   | 0.0         | 0.0           | 0.1      |
|          | Mem. [GB] | 0.3                | 0.2   | 0.5                      | 0.3   | 0.2         | 0.3           | 0.2      |
| 14,400   | It.       | —                  | 8.3   | —                        | 83    | 26          | —             | 22       |
|          | Setup [s] | 0.4                | 6.1   | 1.1                      | 1.1   | 0.6         | 2.1           | 0.6      |
|          | Solve [s] | 3.4                | 0.5   | 7.5                      | 1.9   | 0.1         | 0.2           | 0.4      |
|          | Mem. [GB] | 1.1                | 0.8   | 2.0                      | 0.9   | 0.8         | 1.0           | 0.8      |
| 32,400   | It.       | —                  | 10    | —                        | 93    | 22          | —             | 22       |
|          | Setup [s] | 0.9                | 20    | 3.0                      | 3.0   | 1.8         | 6.2           | 1.9      |
|          | Solve [s] | 11.3               | 1.4   | 24.8                     | 5.2   | 0.3         | 0.7           | 1.1      |
|          | Mem. [GB] | 2.6                | 1.7   | 4.9                      | 2.1   | 1.7         | 2.3           | 1.7      |
| 57,600   | It.       | —                  | 11    | —                        | 100   | 20          | —             | 23       |
|          | Setup [s] | 1.7                | 43    | 6.6                      | 7.1   | 5.1         | 14.2          | 5.2      |
|          | Solve [s] | 24.9               | 2.8   | 51.4                     | 9.7   | 0.5         | 1.2           | 2.2      |
|          | Mem. [GB] | 4.3                | 3.0   | 9.2                      | 3.7   | 3.0         | 4.4           | 3.0      |
| 90,000   | It.       | —                  | 11    | —                        | 105   | 21          | —             | 23       |
|          | Setup [s] | 2.7                | 73    | 9.8                      | 10.0  | 6.8         | 27.8          | 6.9      |
|          | Solve [s] | 58.4               | 4.5   | 109.0                    | 16.6  | 0.8         | 2.3           | 3.5      |
|          | Mem. [GB] | 8.2                | 4.6   | 15.1                     | 5.7   | 4.6         | 6.9           | 4.6      |
| 129,600  | It.       | —                  | 13    | —                        | 111   | 23          | —             | 24       |
|          | Setup [s] | 4.7                | 130   | 20.9                     | 26.5  | 17.9        | 44.7          | 18.5     |
|          | Solve [s] | 91.2               | 8.0   | 185.6                    | 29.4  | 1.4         | 3.8           | 6.5      |
|          | Mem. [GB] | 11.8               | 6.7   | 22.5                     | 8.3   | 6.7         | 10.1          | 6.6      |
| 176,400  | It.       | —                  | 14    | —                        | 114   | 26          | —             | 23       |
|          | Setup [s] | 7.5                | 190   | 38.9                     | 32.9  | 28          | 80.5          | 34.0     |
|          | Solve [s] | 152.4              | 11.5  | 314.4                    | 35.2  | 2.2         | 5.6           | 9.3      |
|          | Mem. [GB] | 16.8               | 9.0   | 31.1                     | 11.3  | 9.0         | 14.3          | 9.0      |

Table 5.1: Performance of different solvers in the first 50 time steps of ( $\Delta t = 10^{-3}$ ). The number of degrees of freedom in the finite element approximation (and thus the number of rows and columns in the system matrix) is about 6 times, 8 times and 4.5 times the number of grid elements, for the phase field, orientation field, and Stokes flow, respectively. The direct solver used for the full systems is UMFPACK [16]. The GMRES solver is taken from dune-istl [7] (**RestartedGMRESolver**) and used without preconditioner for the orientation field systems (both full system matrix and Schur complement, see Section 3.6.2). For the phase field system, we use an incomplete LU factorization of the matrix (3.30) as a preconditioner (using **IncompleteLUT** from the Eigen package [23]). The Stokes schur solver uses a CG solver (dune-istl’s **CGSolver**) preconditioned with the pressure mass matrix [42] to invert the Schur complement. All mass matrices needed in the Schur solvers or for the preconditioners are inverted using the sparse Cholesky factorization (**SimplicialLDLT**) of the Eigen package. All computations are serial (no parallelization). *It.*: Average number of iterations for a single solve, *Setup*: Time needed for initial setup of the solver (mostly factorization of matrices). *Solve*: Average (wall) time needed for a single solve. *Mem.*: Maximum whole-program memory usage (maximum resident set size). For the systems that are not mentioned in the column header, we always use the preconditioned GMRES solver for the phase field system, the Schur solver for the orientation field system and the CG Schur solver preconditioned by the pressure mass matrix for the Stokes system.

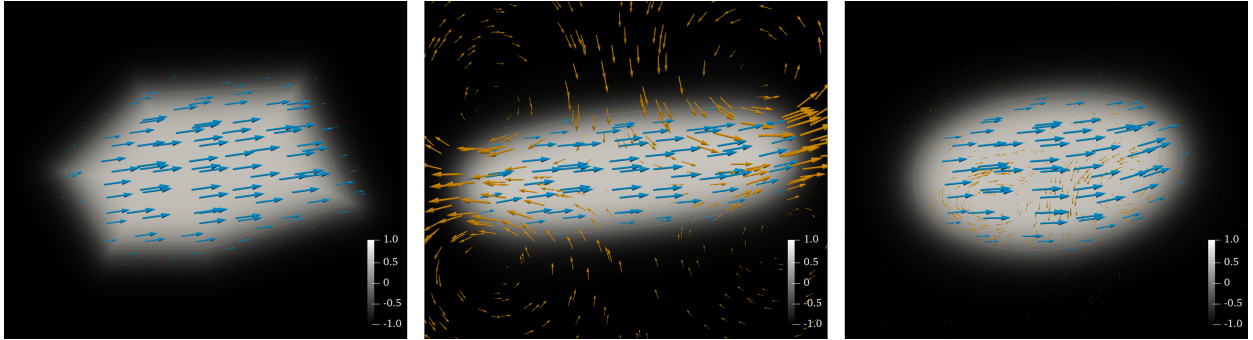


Figure 5.2: Initial values (left) and solution at time  $t = 5$  for  $Ca = 1$  (center) and  $Ca = 0.2$  (right) for the cell isolation test case. The other parameters are chosen as  $Be = Pa = Fa = 1$ . Numerical solutions were computed using the first-order ( $p = 1$ ) finite element discretization from Section 3.4 on a uniform simplicial grid with  $240 \times 240$  elements and a time step of  $\Delta t = 0.001$ . The color bar gives the values of the phase field  $\phi$ . The orientation field  $\mathbf{d}$  and the fluid velocity  $\mathbf{u}$  are represented by blue and orange arrows, respectively.

We use the cell isolation setup from the previous section. We only vary the two parameters  $Ca$  and  $Pa$  by an order of magnitude around 1 such that the parameter space is  $\mathcal{P} = [\frac{1}{\sqrt{10}}, \sqrt{10}]^2$ . We use 32 MPI ranks on a single compute node and sample each parameter uniformly by 8 values ( $n_{train} = 64$ ) such that each MPI rank computes solutions for two parameters. To compute the errors, we randomly choose 32 new parameters (1 parameter per rank) and compute both full-order and reduced solutions for these parameters. As error measures, we use the absolute and relative mean  $L^2$  errors

$$\bar{E}_{\text{abs}}^2 = \left( \frac{1}{|\mathcal{S}|} \sum_{\mathbf{v} \in \mathcal{S}} \|\mathbf{v} - P_{\text{colspan}} \mathbf{U}(\mathbf{v})\|_W^2 \right)^{\frac{1}{2}}, \quad \bar{E}_{\text{rel}}^2 = \left( \frac{1}{|\mathcal{S}|} \sum_{\mathbf{v} \in \mathcal{S}} \frac{\|\mathbf{v} - P_{\text{colspan}} \mathbf{U}(\mathbf{v})\|_W^2}{\|\mathbf{v}\|_W^2} \right)^{\frac{1}{2}}. \quad (5.1)$$

The results without DEIM can be found in Figures 5.3 to 5.5. We see that both relative and absolute error for all fields are proportional to the prescribed tolerance, except for the very low tolerance  $10^{-7}$  (probably due to numerical inaccuracies). In all cases, the error for the approximated field is about an order of magnitude larger than the induced error in the other fields. We can thus conclude that the errors are not amplified between equations. Regarding the absolute values, we see that, at least for the smaller tolerances, the error (in the Stokes variables) introduced by the Stokes approximation is about an order of magnitude smaller than the errors introduced by the phase field and orientation field approximations in their respective variables. In the following, we thus might have to choose the tolerances for these fields about an order of magnitude smaller than the Stokes tolerance.

The maximal number of local modes, the maximal number of input vectors to a local POD and the number of final POD modes are similar for the three fields.

To analyse the effect of the DEIM hyperreduction, we then fix the tolerance for the snapshot POD to  $10^{-5}$  and perform the same computations again, this time with added DEIM hyperreduction for different prescribed tolerances. As can be seen in Figures 5.6 to 5.8, for DEIM tolerance small enough the errors are basically independent of the DEIM tolerance and similar to the errors without DEIM hyperreduction (compare results for a tolerance of  $10^{-5}$  in Figures 5.3 to 5.5). However, if the DEIM is increased, there is a point where the DEIM interpolation becomes insufficient and the errors jump by several orders of magnitude. For the phase field, for a POD tolerance of  $10^{-5}$ , this jump occurs at a DEIM tolerance between  $5 \cdot 10^{-9}$  and  $10^{-8}$ , for the orientation field between  $10^{-8}$  and  $10^{-7}$  and for the Stokes variables between  $10^{-7}$  and  $10^{-6}$ . These results indicate that the optimal DEIM tolerance for a POD tolerance of  $10^{-5}$  is in the order of  $10^{-8}$ . For larger tolerances, large errors can be observed, and further decreasing the tolerance is inefficient since it increase the number of DEIM modes without improving the model reduction errors.

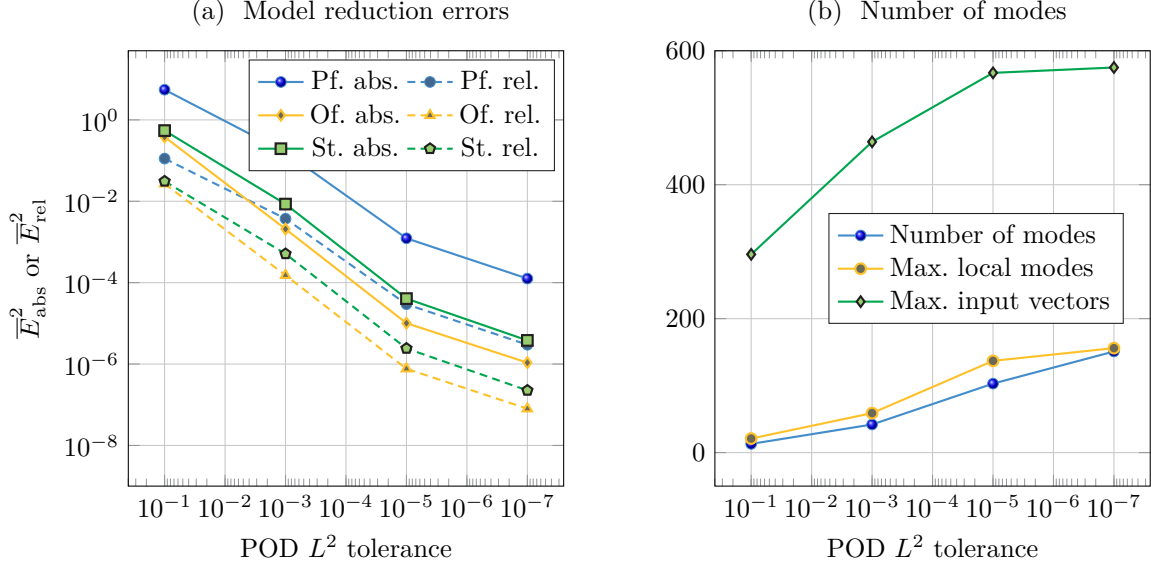


Figure 5.3: Errors and number of modes used for HAPOD approximation of the phase field with different prescribed tolerances (cell isolation test case,  $80 \times 80$  rectangular grid,  $t_f = 0.2$ ,  $\Delta t = 0.001$ ,  $\omega = 0.95$ ). (a) Mean  $L^2$  model reduction error in the different fields. (b) Number of modes obtained from the HAPOD.

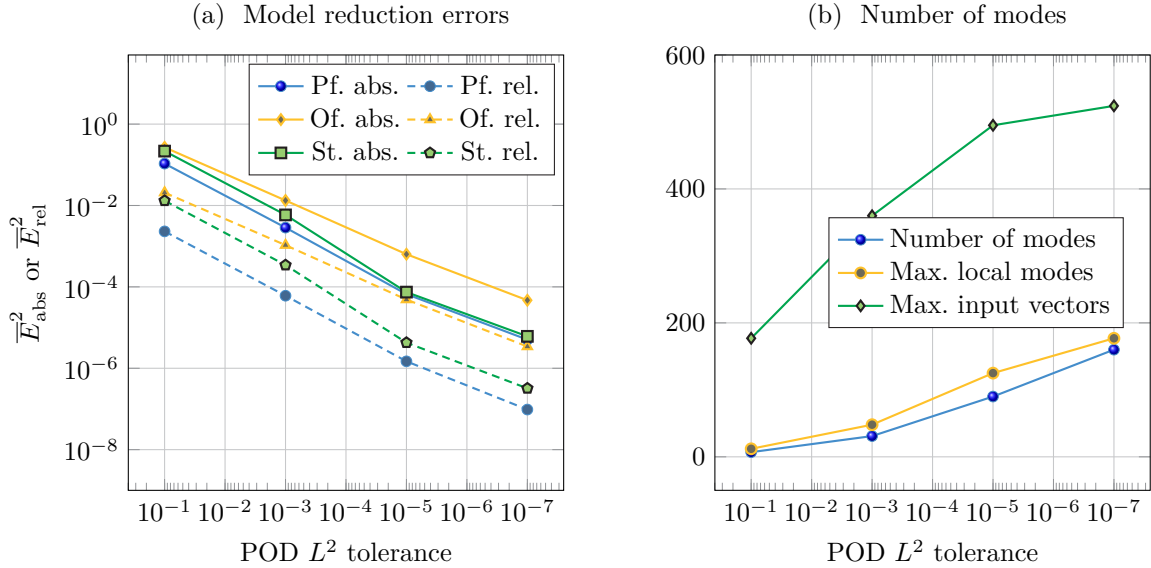


Figure 5.4: Errors and number of modes used for HAPOD approximation of the orientation field with different prescribed tolerances (cell isolation test case,  $80 \times 80$  rectangular grid,  $t_f = 0.2$ ,  $\Delta t = 0.001$ ,  $\omega = 0.95$ ). (a) Mean  $L^2$  model reduction error in the different fields. (b) Number of modes obtained from the HAPOD.

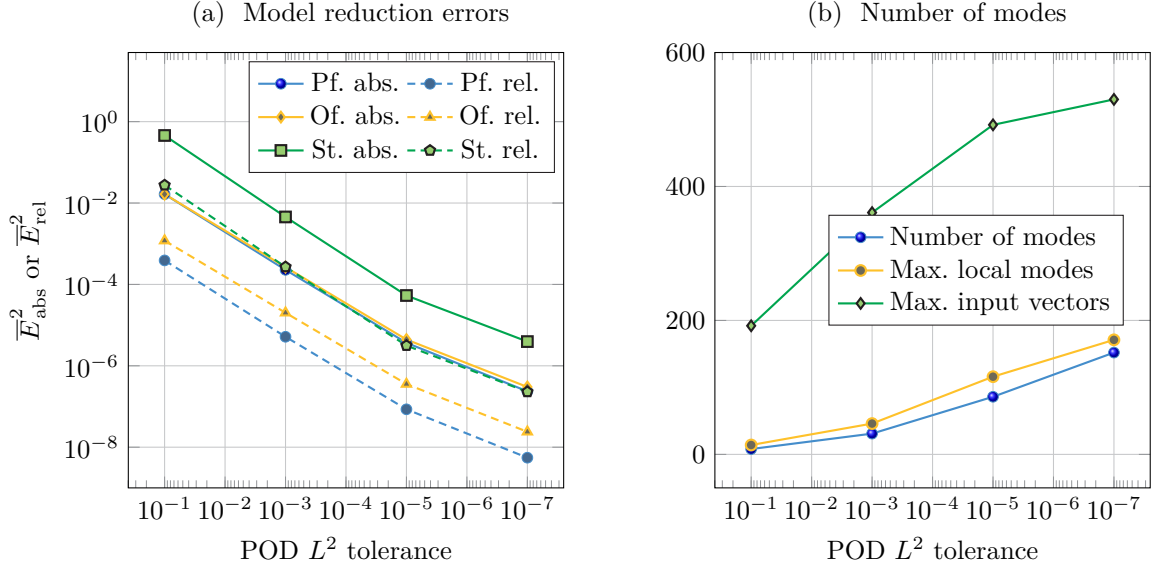


Figure 5.5: Errors and number of modes used for HAPOD approximation of the Stokes field with different prescribed tolerances (cell isolation test case,  $80 \times 80$  rectangular grid,  $t_f = 0.2$ ,  $\Delta t = 0.001$ ,  $\omega = 0.95$ ). (a) Mean  $L^2$  model reduction error in the different fields. (b) Number of modes obtained from the HAPOD.

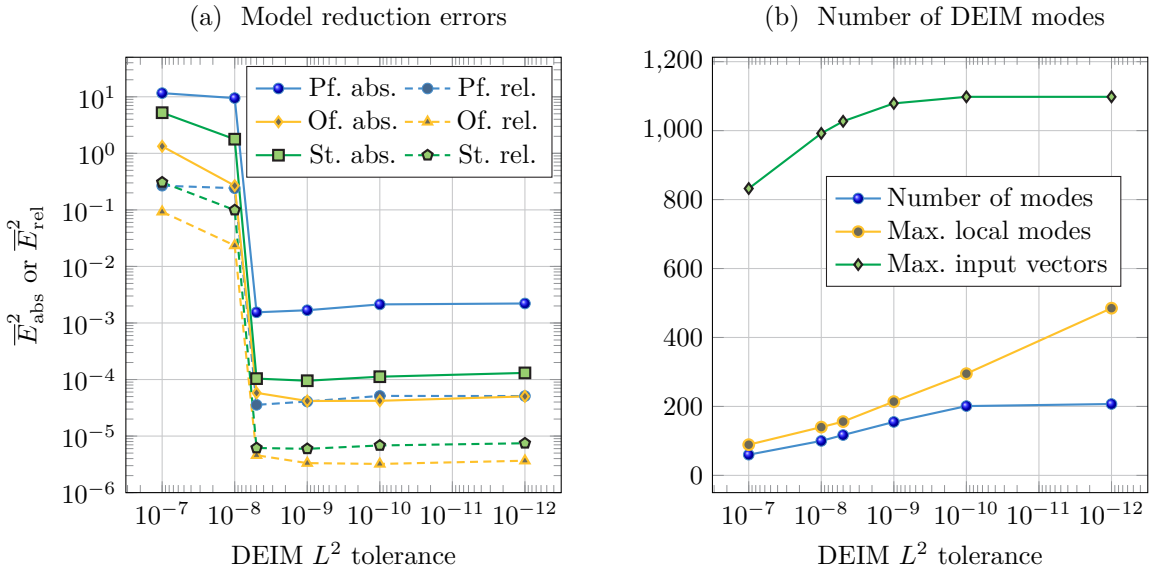


Figure 5.6: Errors and number of DEIM modes used for HAPOD-DEIM approximation of the phase field using a fixed prescribed tolerance of  $10^{-5}$  for the POD and varying DEIM tolerances (cell isolation test case,  $80 \times 80$  rectangular grid,  $t_f = 0.2$ ,  $\Delta t = 0.001$ ,  $\omega = 0.95$ ). (a) Mean  $L^2$  model reduction error in the different fields. (b) Number of DEIM modes obtained from the HAPOD.

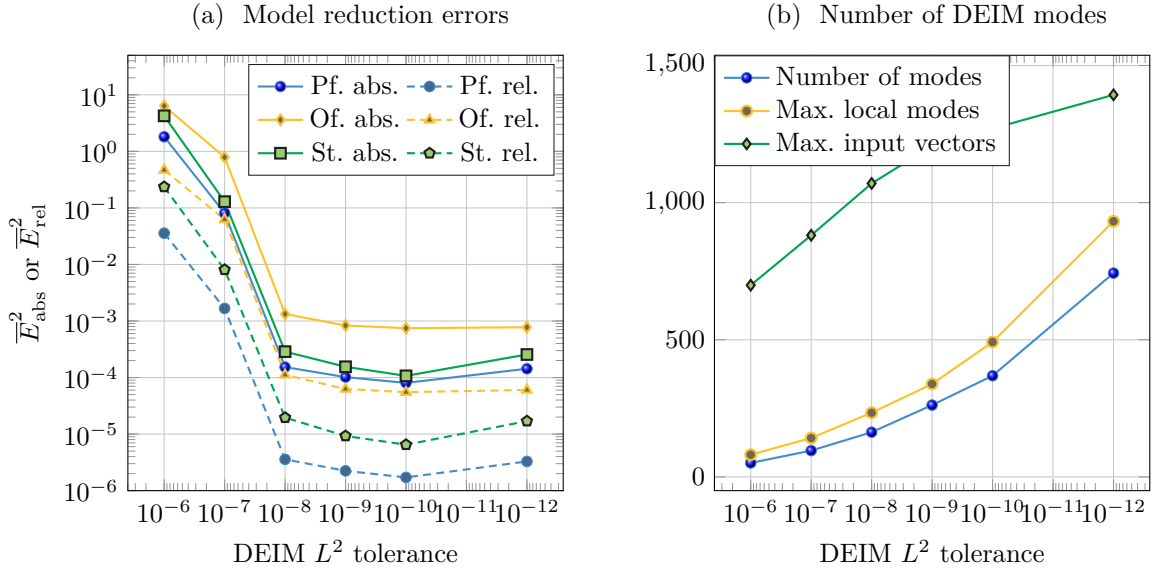


Figure 5.7: Errors and number of DEIM modes used for HAPOD-DEIM approximation of the orientation field using a fixed prescribed tolerance of  $10^{-5}$  for the POD and varying DEIM tolerances (cell isolation test case,  $80 \times 80$  rectangular grid,  $t_f = 0.2$ ,  $\Delta t = 0.001$ ,  $\omega = 0.95$ ). (a) Mean  $L^2$  model reduction error in the different fields. (b) Number of DEIM modes obtained from the HAPOD.

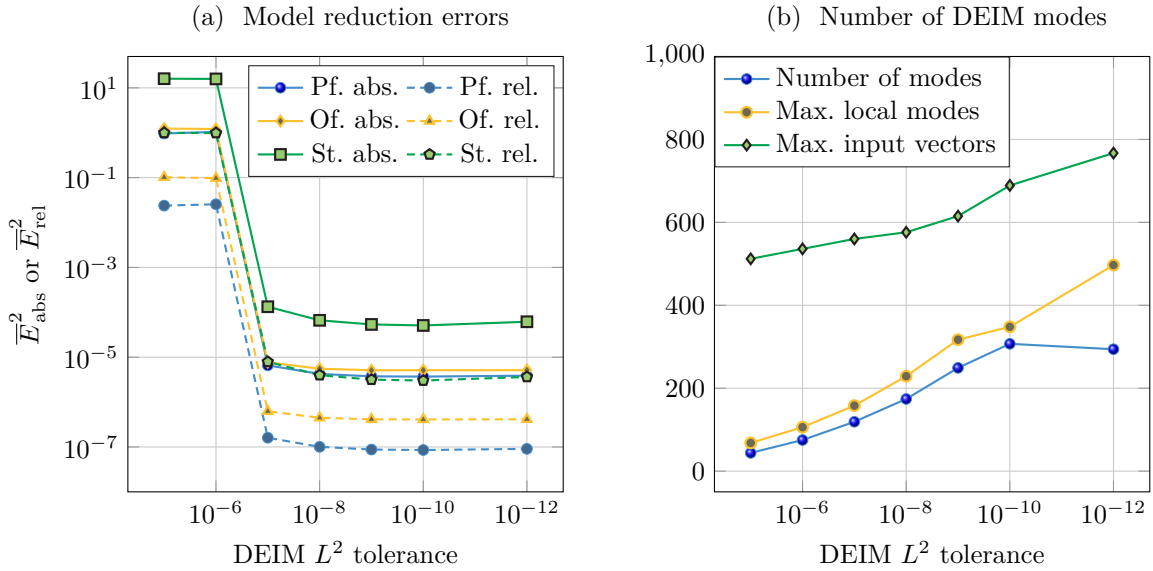


Figure 5.8: Errors and number of DEIM modes used for HAPOD-DEIM approximation of the Stokes variables using a fixed prescribed tolerance of  $10^{-5}$  for the POD and varying DEIM tolerances (cell isolation test case,  $80 \times 80$  rectangular grid,  $t_f = 0.2$ ,  $\Delta t = 0.001$ ,  $\omega = 0.95$ ). (a) Mean  $L^2$  model reduction error in the different fields. (b) Number of DEIM modes obtained from the HAPOD.

## 6. Conclusion and Outlook

We suggested to use a nonlinear continuum approach to model microtubule-based forces in planar fruit fly wing tissues. We presented preconditioned iterative solvers for the discretized model and outlined an approach to obtain reduced models that can be used, e.g. to make parameter studies possible where the model has been solved repeatedly for many different parameters. We proposed to use the hierarchical approximate POD (HAPOD) to efficiently compute the reduced bases needed for the model reduction and for an additional hyperreduction by the discrete empirical interpolation method (DEIM). Finally, we presented some first numerical studies on the choice of tolerances for the basis construction showing that a sufficiently efficient approximation can be obtained with a reasonably small number of reduced basis functions for each variable. By now, we only reduced one of the equations at a time. Since the other variables are still high-dimensional, we cannot expect that the reduced model is significantly faster than the full-order model in this setting. To get an actual speed-up, we have to reduce all of the three equations. Preliminary results indicate that a speed-up of about 100x can realistically be achieved.

## Acknowledgement

We acknowledge funding by the Deutsche Forschungsgemeinschaft under Germany's Excellence Strategy EXC 2044-390685587, Mathematics Münster: Dynamics – Geometry – Structure (T. Leibner, M. Ohlberger, S. Rave) and EXC 1003 FF-2015-07 (T. Leibner, M. Matis, M. Ohlberger).

## References

- [1] B. ALBERTS, D. BRAY, K. HOPKIN, A. JOHNSON, J. LEWIS, M. RAFF, K. ROBERTS, AND P. WALTER, eds., *Essential cell biology*, Garland Science, New York, NY, 4 ed., 2014.
- [2] S. P. BANAVAR, E. K. CARN, P. ROWGHANIAN, G. STOOKE-VAUGHAN, S. KIM, AND O. CAMPÀS, *Mechanical control of tissue shape and morphogenetic flows during vertebrate body axis elongation*, Scientific reports, 11 (2021), p. 8591, <https://doi.org/10.1038/s41598-021-87672-3>.
- [3] M. BARRAULT, Y. MADAY, N. NGUYEN, AND A. PATERA, *An ‘empirical interpolation’ method: application to efficient reduced-basis discretization of partial differential equations*, Comptes Rendus Mathématique, 339 (2004), pp. 667–672.
- [4] P. BENNER, A. COHEN, M. OHLBERGER, AND K. WILLCOX, eds., *Model reduction and approximation*, vol. 15 of Computational Science & Engineering, Society for Industrial and Applied Mathematics (SIAM), Philadelphia, PA, 2017, <https://doi.org/10.1137/1.9781611974829>, <https://doi.org/10.1137/1.9781611974829>. Theory and algorithms.
- [5] P. BENNER, M. OHLBERGER, A. PATERA, G. ROZZA, AND K. URBAN, eds., *Model reduction of parametrized systems*, vol. 17 of MS&A. Modeling, Simulation and Applications, Springer, Cham, 2017, <https://doi.org/10.1007/978-3-319-58786-8>, <https://doi.org/10.1007/978-3-319-58786-8>. Selected papers from the 3rd MoRePaS Conference held at the International School for Advanced Studies (SISSA), Trieste, October 13–16, 2015.
- [6] M. BENZI, G. H. GOLUB, AND J. LIESEN, *Numerical solution of saddle point problems*, Acta Numerica, 14 (2005), p. 1–137, <https://doi.org/10.1017/S0962492904000212>.
- [7] M. BLATT AND P. BASTIAN, *The iterative solver template library*, in Applied Parallel Computing – State of the Art in Scientific Computing, B. Kagström, E. Elmroth, J. Dongarra, and J. Wasniewski, eds., Berlin/Heidelberg, 2007, Springer, pp. 666–675.
- [8] B. P. BOUCHET AND A. AKHMANOVA, *Microtubules in 3d cell motility*, Journal of cell science, 130 (2017), pp. 39–50.
- [9] P. BOYANOVA, M. DO-QUANG, AND M. NEYTCHIEVA, *Solution methods for the Cahn-Hilliard equation discretized by conforming and non-conforming finite elements*, Tech. Report 2011-004, Department of Information Technology, Uppsala University, Mar. 2011.
- [10] G. W. BRODLAND, *How computational models can help unlock biological systems*, Seminars in Cell & Developmental Biology, 47-48 (2015), pp. 62–73, <https://doi.org/10.1016/j.semcd.2015.07.001>.
- [11] J. W. CAHN AND J. E. HILLIARD, *Free energy of a nonuniform system. i. interfacial free energy*, Journal of Chemical Physics, 28 (1958), pp. 258–267, <https://doi.org/10.1063/1.1744102>, <https://ui.adsabs.harvard.edu/abs/1958JChPh..28..258C>.
- [12] J. W. CAHN AND J. E. HILLIARD, *Free energy of a nonuniform system. iii. nucleation in a two-component incompressible fluid*, Journal of Chemical Physics, 31 (1959), pp. 688–699, <https://doi.org/10.1063/1.1730447>, <https://ui.adsabs.harvard.edu/abs/1959JChPh..31..688C>.
- [13] S. CHATURANTABUT AND D. C. SORENSEN, *Nonlinear model reduction via discrete empirical interpolation*, SIAM Journal on Scientific Computing, 32 (2010), pp. 2737–2764, <https://doi.org/10.1137/090766498>.

- [14] P. CIARLETTA, T. HILLEN, H. OTHMER, L. PREZIOSI, AND D. TRUCU, *Mathematical models and methods for living systems*, vol. 2167 of Lecture Notes in Mathematics, Springer, [Cham]; Centro Internazionale Matematico Estivo (C.I.M.E.), Florence, 2016, <https://doi.org/10.1007/978-3-319-42679-2>, <https://doi.org/10.1007/978-3-319-42679-2>. Lectures from the C.I.M.E.-C.I.R.M. Summer School held in Levico Terme, 2014, Edited by Preziosi, Mark Chaplain and Andrea Pugliese, Fondazione CIME/CIME Foundation Subseries.
- [15] A. D'ANGELO, K. DIERKES, C. CAROLIS, G. SALBREUX, AND J. SOLON, *In vivo force application reveals a fast tissue softening and external friction increase during early embryogenesis.*, *Current biology : CB*, 29 (2019), pp. 1564–1571.e6, <https://doi.org/10.1016/j.cub.2019.04.010>.
- [16] T. A. DAVIS, *Algorithm 832: Umfpack v4.3—an unsymmetric-pattern multifrontal method*, *ACM Trans. Math. Softw.*, 30 (2004), p. 196–199, <https://doi.org/10.1145/992200.992206>, <https://doi.org/10.1145/992200.992206>.
- [17] S. R. DE GROOT AND P. MAZUR, *Non-equilibrium thermodynamics*, Courier Corporation, 2013.
- [18] M. DROHMANN, B. HAASDONK, AND M. OHLBERGER, *Reduced basis approximation for nonlinear parametrized evolution equations based on empirical operator interpolation*, *SIAM J. Sci. Comput.*, 34 (2012), pp. 937–969.
- [19] H. FAN AND S. LI, *Modeling microtubule cytoskeleton via an active liquid crystal elastomer model*, *Computational Materials Science*, 96 (2015), pp. 559–566, <https://doi.org/10.1016/j.commatsci.2014.04.041>. Special Issue Polymeric Composites.
- [20] P. C. FIFE, *Models for phase separation and their mathematics*, *Electronic Journal of Differential Equations*, 2000 (2000), pp. 1–26, <http://ejde.math.txstate.edu/Volumes/2000/48/abstr.html>.
- [21] D. A. FLETCHER AND R. D. MULLINS, *Cell mechanics and the cytoskeleton.*, *Nature*, 463 (2010), pp. 485–492, <https://doi.org/10.1038/nature08908>.
- [22] B. GMEINER, U. RÜDE, H. STENDEL, C. WALUGA, AND B. WOHLMUTH, *Performance and scalability of hierarchical hybrid multigrid solvers for Stokes systems*, *SIAM Journal on Scientific Computing*, 37 (2015), pp. C143–C168, <https://doi.org/10.1137/130941353>.
- [23] G. GUENNEBAUD, B. JACOB, ET AL., *Eigen v3*. <http://eigen.tuxfamily.org>, 2010, <https://eigen.tuxfamily.org>.
- [24] B. HAASDONK AND M. OHLBERGER, *Reduced basis method for finite volume approximations of parametrized linear evolution equations*, *M2AN Mathematical Modelling and Numerical Analysis*, 42 (2008), pp. 277–302.
- [25] F. HAUSSER, S. LI, J. LOWENGRUB, W. MARTH, A. RÄTZ, AND A. VOIGT, *Thermodynamically consistent models for two-component vesicles*, *International Journal of Biomathematics and Biostatistics*, 2 (2013).
- [26] W. HELFRICH, *Elastic properties of lipid bilayers: Theory and possible experiments*, *Zeitschrift für Naturforschung C*, 28 (1973), pp. 693–703, <https://doi.org/doi:10.1515/znc-1973-11-1209>, <https://doi.org/10.1515/znc-1973-11-1209>.
- [27] J. S. HESTHAVEN, G. ROZZA, AND B. STAMM, *Certified reduced basis methods for parametrized partial differential equations*, *SpringerBriefs in Mathematics*, Springer International Publishing, 2016.
- [28] C. HIMPE, T. LEIBNER, AND S. RAVE, *Hierarchical approximate proper orthogonal decomposition*, *SIAM Journal on Scientific Computing*, 40 (2018), pp. A3267–A3292, <https://doi.org/10.1137/16M1085413>.
- [29] D. E. INGBER, N. WANG, AND D. STAMENOVIĆ, *Tensegrity, cellular biophysics, and the mechanics of living systems*, *Reports on Progress in Physics*, 77 (2014), p. 046603, <https://doi.org/10.1088/0034-4885/77/4/046603>, <https://doi.org/10.1088/0034-4885/77/4/046603>.
- [30] E. D. KORN, *Biochemistry of actomyosin-dependent cell motility (a review)*, *Proceedings of the National Academy of Sciences*, 75 (1978), pp. 588–599, <https://doi.org/10.1073/pnas.75.2.588>, <https://www.pnas.org/content/75/2/588>, <https://arxiv.org/abs/https://www.pnas.org/content/75/2/588.full.pdf>.
- [31] K. KRUSE, J. F. JOANNY, F. JÜLICHER, J. PROST, AND K. SEKIMOTO, *Generic theory of active polar gels: a paradigm for cytoskeletal dynamics*, *The European Physical Journal E*, 16 (2005), pp. 5–16, <https://doi.org/10.1140/epje/e2005-00002-5>.
- [32] K. KRUSE, J. F. JOANNY, F. JÜLICHER, J. PROST, AND K. SEKIMOTO, *Generic theory of active polar gels: a paradigm for cytoskeletal dynamics.*, *The European physical journal. E, Soft matter*, 16 (2005), pp. 5–16, <https://doi.org/10.1140/epje/e2005-00002-5>.
- [33] B. LADOUX, R.-M. MÈGE, AND X. TREPAT, *Front–rear polarization by mechanical cues: From single cells to tissues*, *Trends in Cell Biology*, 26 (2016), pp. 420 – 433, <https://doi.org/https://doi.org/10.1016/j.tcb.2016.02.002>, <http://www.sciencedirect.com/science/article/pii/S0962892416000143>.
- [34] D. LEE, J.-Y. HUH, D. JEONG, J. SHIN, A. YUN, AND J. KIM, *Physical, mathematical, and numerical derivations of the cahn–hilliard equation*, *Computational Materials Science*, 81 (2014), pp. 216 – 225, <https://doi.org/https://doi.org/10.1016/j.commatsci.2013.08.027>, <http://www.sciencedirect.com/science/article/pii/S0927025613004801>.
- [35] M. C. MARCHETTI, J. F. JOANNY, S. RAMASWAMY, T. B. LIVERPOOL, J. PROST, M. RAO, AND R. A. SIMHA, *Hydrodynamics of soft active matter*, *Reviews of Modern Physics*, 85 (2013), pp. 1143–1189, <https://doi.org/10.1103/RevModPhys.85.1143>, <https://ui.adsabs.harvard.edu/abs/2013RvMP...85.1143M>.
- [36] W. MARTH, *Hydrodynamic Diffuse Interface Models for Cell Morphology and Motility*, phdthesis, TU Dresden, 2016.
- [37] W. MARTH, S. PRAETORIUS, AND A. VOIGT, *A mechanism for cell motility by active polar gels*, *Journal of The Royal Society Interface*, 12 (2015), p. 20150161.
- [38] M. MATIS, *The mechanical role of microtubules in tissue remodeling*, *BioEssays*, 42 (2020), p. 1900244, <https://doi.org/10.1002/bies.201900244>.
- [39] F. MEITINGER AND S. PALANI, *Actomyosin ring driven cytokinesis in budding yeast*, *Seminars in Cell And Developmental Biology*, 53 (2016), pp. 19 – 27, <https://doi.org/https://doi.org/10.1016/j.semdb.2016.01.043>, <http://www.sciencedirect.com/science/article/pii/S1084952116300404>. Cytokinetic ring construction and constriction Fibroblast Growth factor signalling.
- [40] P. PANDYA, J. L. ORGAZ, AND V. SANZ-MORENO, *Actomyosin contractility and collective migration: may the force be*

- with you, *Current Opinion in Cell Biology*, 48 (2017), pp. 87 – 96, <https://doi.org/https://doi.org/10.1016/j.ceb.2017.06.006>, <http://www.sciencedirect.com/science/article/pii/S0955067417300261>. *Cell Dynamics*.
- [41] R. J. PELLHAM AND F. CHANG, *Actin dynamics in the contractile ring during cytokinesis in fission yeast*, *Nature*, 419 (2002), pp. 82–86, <https://doi.org/10.1038/nature00999>.
- [42] J. PETERS, V. REICHEL, AND A. REUSKEN, *Fast iterative solvers for discrete stokes equations*, *SIAM Journal on Scientific Computing*, 27 (2005), pp. 646–666, <https://doi.org/10.1137/040606028>.
- [43] T. D. POLLARD AND J. A. COOPER, *Actin, a central player in cell shape and movement*, *Science*, 326 (2009), pp. 1208–1212, <https://doi.org/10.1126/science.1175862>.
- [44] A. QUARTERONI, *Numerical models for differential problems*, 2017, <http://dx.doi.org/10.1007/978-3-319-49316-9>.
- [45] A. QUARTERONI, A. MANZONI, AND F. NEGRI, *Reduced basis methods for partial differential equations*, vol. 92 of *Unitext*, Springer, Cham, 2016, <https://doi.org/10.1007/978-3-319-15431-2>. An introduction, *La Matematica per il 3+2*.
- [46] R. RAPPAPORT, *Cytokinesis in animal cells*, Cambridge University Press, 1996.
- [47] D. N. ROBINSON AND J. A. SPUDICH, *Towards a molecular understanding of cytokinesis*, *Trends in cell biology*, 10 (2000), pp. 228–237.
- [48] G. SALBREUX, G. CHARRAS, AND E. PALUCH, *Actin cortex mechanics and cellular morphogenesis*, *Trends in cell biology*, 22 (2012), pp. 536–545.
- [49] A. SINGH, T. SAHA, I. BEGEMANN, A. RICKER, H. NÜSSE, O. THORN-SESHOLD, J. KLINGAUF, M. GALIC, AND M. MATIS, *Polarized microtubule dynamics directs cell mechanics and coordinates forces during epithelial morphogenesis*, *Nature Cell Biology*, 20 (2018), pp. 1126–1133, <https://doi.org/10.1038/s41556-018-0193-1>.
- [50] L. SIROVICH, *Turbulence and the dynamics of coherent structures part I: Coherent structures*, *Quarterly of Applied Mathematics*, 45 (1987), pp. 561–571, <http://www.jstor.org/stable/43637457>.
- [51] J. SQUIRE, *Special issue: The actin-myosin interaction in muscle: Background and overview*, *International Journal of Molecular Sciences*, 20 (2019), p. 5715, <https://doi.org/10.3390/ijms20225715>.
- [52] E. TJHUNG, D. MARENDUZZO, AND M. E. CATES, *Spontaneous symmetry breaking in active droplets provides a generic route to motility*, *PNAS*, 109 (2012), pp. 12381–12386, <https://doi.org/10.1073/pnas.1200843109>.
- [53] C. VERDIER, J. ETIENNE, A. DUPERRAY, AND L. PREZIOSI, *Review: Rheological properties of biological materials*, *Comptes Rendus Physique*, 10 (2009), pp. 790–811, <https://doi.org/10.1016/j.crhy.2009.10.003>.